EFFORTS TOWARDS THE DESIGN AND DEVELOPMENT OF AN ELECTROMAGNETIC

INDUCTION SENSOR OPTIMIZED FOR DETECTION AND DISCRIMINATION OF

UNEXPLODED ORDNANCE

Except where reference is made to the work of others, the work described in this thesis is my own or was done in collaboration with my advisory committee. This thesis does not include proprietary or classified information.

_____
Jithendra N Palasagaram

Certificate of Approval:

_____   _____
Sadasiva M. Rao   Lloyd S. Riggs, Chair
Professor   Professor
Electrical and Computer Engineering   Electrical and Computer Engineering

_____   _____
Ramesh Ramadoss   Stephen L. McFarland
Assistant Professor   Dean
Electrical and Computer Engineering   Graduate School

EFFORTS TOWARDS THE DESIGN AND DEVELOPMENT OF AN ELECTROMAGNETIC

INDUCTION SENSOR OPTIMIZED FOR DETECTION AND DISCRIMINATION OF

UNEXPLODED ORDNANCE

Jithendra N Palasagaram

A Thesis

Submitted to

the Graduate Faculty of

Auburn University

in Partial Fulfillment of the

Requirements for the

Degree of

Master of Science

Auburn, Alabama
May 11, 2006

EFFORTS TOWARDS THE DESIGN AND DEVELOPMENT OF AN ELECTROMAGNETIC

INDUCTION SENSOR OPTIMIZED FOR DETECTION AND DISCRIMINATION OF

UNEXPLODED ORDNANCE

Jithendra N Palasagaram

_____
Signature of Author

_____
Date of Graduation

VITA

Jithendra N Palasagaram, son of Nagarajeswara Rao P, and Rajamma P, was born on November 15, 1979 in Miryalguda, India. After finishing high school from Crescent Jr. College in 1997, he attended Bangalore University, India where he received his Bachelor of Engineering (Electronics and Communication) degree in 2001. He entered graduate school at Auburn University in Fall of 2003 as a graduate research assistant, and later went on to accept a fellowship through Auburn University.

THESIS ABSTRACT

EFFORTS TOWARDS THE DESIGN AND DEVELOPMENT OF AN ELECTROMAGNETIC

INDUCTION SENSOR OPTIMIZED FOR DETECTION AND DISCRIMINATION OF

UNEXPLODED ORDNANCE

Jithendra N Palasagaram

Master of Science, May 11, 2006
(B. E., Golden Valley Institute of Technology, Bangalore University, 2001)

101 Typed Pages

Directed by Dr. Lloyd S. Riggs

This thesis provides a detailed description of efforts towards the development of a time

domain electromagnetic induction (EMI) system optimized for detection and

discrimination of Unexploded Ordnance (UXO). A time domain (or pulsed) EMI system

with good discrimination capability must be able to accurately capture a UXO target's

late-time response. Here, late-time response is defined as the time period starting a few

hundred microseconds after the transmitter current turn off and extending to

approximately 20 milliseconds or to just before the beginning of the next transmitter

current pulse. A pulsed EMI system must have sufficient bandwidth, especially at the

lower end, to accurately measure a UXO target's late time response. EMI system

components include transmitter and receiver coils and corresponding transmitter and

receiver coil amplifiers as well as the data acquisition system (analogue-to-digital converter). This thesis addresses EMI system component design and tradeoffs necessary to achieve the bandwidth and sensitivity for good UXO detection and discrimination performance.

Field measurements were taken at the Blossom Point Test Site in Maryland in order to evaluate the detection and discrimination performance of the pulsed EMI sensor. Although overall performance was good, several deficiencies were noted. In particular, the low 3dB frequency of the receiver coil amplifier was inadvertently set too high (above 1 kHz) which resulted in a prematurely truncated late-time response. In short, we did not observe the expected long exponential "tails" indicative of larger ferrous test targets. This problem has recently been corrected using a current-to-voltage converter as the first amplification stage following the receiver coil. The current-to-voltage converter has very low input impedance so that the system lower 3 dB frequency is fixed solely by the resistance-inductance ratio of the receiver coil (currently set to 80 Hz).

Testing also indicated a deficiency in system sensitivity. This problem has been attributed to insufficient receiver coil moment; specifically, the area of each half of the currently employed bucking receiver coil is too small. Future plans are to replace each 1 ft^2 half of the bucking receiver coils with a vertically stacked arrangement of two 1 m^2 coils, one above and the other below the transmitter coil. The moment of the new coils will increase by a factor of 10 over that of the old and thus overall sensitivity should increase by the same factor. Additionally, future plans include purchasing a 1 kW transmitter coil amplifier capable of delivering over 40 amps at rated voltage (22.5 V rms). The transmitter coil amplifier used in the Blossom Point tests delivered a peak

current of less than 20 amps so the new amplifier, all other system parameters held constant, should improve overall sensitivity by more than 3 dB.

Of course sensitivity can be improved by either increasing the received signal level or by reducing noise. A "boot strapped" differential amplifier has been tested that has significantly improved noise performance compared to the previously used single ended amplifier. Furthermore, testing is currently underway to evaluate a three operational amplifier configuration that should even further reduce noise yet still have very low input impedance and thus very good low frequency performance.

Lastly, during the Blossom Point tests some problems were encountered with the test cart wheel bearings. At the very least we plan to replace the "home made" PVC wheel bearings with manufactured bearings. We learned about the source of the manufactured bearings from a colleague at a recent UXO workshop.

In addition to the description of efforts towards the development of an EMI sensor optimized for detection and discrimination of UXO, a brief description of the efforts towards the development of a Microelectromechanical Systems (MEMS) Capacitive Pressure Sensor Array fabricated using Printed circuit processing techniques is also presented in this thesis. MEMS capacitive pressure sensors are usually fabricated using silicon micromachining techniques. In this work, novel Liquid Crystal Polymer (LCP) based capacitive pressure sensors fabricated using printed circuit processing techniques are presented. The design, fabrication and experimental characterization of the sensor are presented.

Style manual of journal used Graduate School: Guide to preparation and
submission of theses and dissertations

Computer software used Microsoft Office XP

TABLE OF CONTENTS

LIST OF FIGURES

LIST OF TABLES

CHAPTER 1 INTRODUCTION

Unexploded ordnance (UXO) is explosive ordnance that, due to some malfunction remains undetonated. Usually, they are long thin rod like structures, which can range in size from 20mm shells to 2000 lb bombs. UXO may be clearly visible, hidden in undergrowth, or buried beneath the ground.

UXO is recognized as one of the world's most serious and dangerous environmental problems. The presence of UXO has an economic impact on the livelihood of many people across the world and also deters the reconstruction and development efforts of war torn countries. The majority of the casualties caused by UXO are comprised of civilians and children, who work for livelihood in areas which were once battlefields and /or military testing areas.

According to *Landmine Monitor Report 2004* [1], around two-thirds of the countries in the world – 121 countries – are affected to some extent by the landmine/UXO problem. New landmine/UXO casualties were reported in 66 countries. 1,833 of these deaths were children, approximately 23% of the total casualties reported. Less than 14 percent of reported casualties were identified as active military personnel. These numbers do not take into account the many unreported casualties, as innocent civilians are killed or injured in remote areas away from any form of assistance or means of communication.

In many Mine/UXO affected countries the assistance available to address the needs of survivors is inadequate. Most of the survivors do not have access to some of the basic needs like food security, access to water, roads, adequate housing, and a way to earn an income. The social and economic impact of Mines/UXO on the lives of these people and their countries serve to emphasize the need for humanitarian landmine/UXO removal [1].

The United States Department of Defense estimates that there are nearly 15 million acres of ranges contaminated with UXO [2]. In recent years there has been a considerable effort to clear these UXO contaminated areas. However, current methods used are time consuming, expensive and present a great risk to the personnel involved. Funding has been provided by the Environmental Security Technology Certification Program (ESTCP), and the Strategic Environmental Research and Development Program (SERDP) to address the technology needed to improve the detection and discrimination of landmine/UXO items and also ensure the safety of the personnel involved.

With a SERDP funded grant, our research team at Auburn University is involved in the development of an Electromagnetic Induction Sensor optimized for UXO detection, and classification. Previous work at Auburn University and elsewhere has shown that EMI has the potential for detection and classification [3], [4].

This thesis will address the key topics related to an EMI sensor optimized for the purpose of detection and discrimination of UXO. The focus is to concentrate on developing low frequency (late time) EMI techniques in the characterization of thin and thick-walled UXO like items and UXO. This research is divided into four parts: In CHAPTER 2, a brief description of the theory of an EMI system is presented followed by

a description of the two types of EMI systems: Time Domain (Pulsed) EMI and Frequency Domain (Continuous Wave) EMI sensor. In CHAPTER 3, the issues related to the design of the transmitter and receiver coils, the signal processing circuitry, and data acquisition hardware are presented. In CHAPTER 4, data collection of the desired targets in the lab, and also the data obtained from the field measurements carried out at the Naval Research Laboratory's Blossom Point Test Site in Maryland are presented and analyzed. A detailed description of the field tests is presented in APPENDIX A.

CHAPTER 5 summarizes the research work followed by suggestions for future efforts.

In addition to the work described above, a brief description of a MEMS capacitive pressure sensor array fabricated using printed circuit processing techniques is presented in this thesis. MEMS capacitive pressure sensors are usually fabricated using silicon micromachining techniques [20]. In this work, novel Liquid Crystal Polymer (LCP) based capacitive pressure sensors fabricated using printed circuit processing techniques are presented. The advantages of using LCP include low cost, versatility of fabrication such as low temperature thermal bonding, mechanical flexibility, less moisture absorption compared to other polymer films used in MEMS processes [21]. Further details are provided in APPENDIX B.

CHAPTER 2   THEORY OF ELECTROMAGNETIC INDUCTION SENSOR

2.1 Introduction

In the previous chapter, the need for the development of an EMI system for detection and discrimination of UXO was discussed. This chapter provides the reader with the basic concepts of an EMI system. This chapter is organized as follows: The configuration and principle of a basic EMI system [5], [6] are discussed. Next, the different types of EMI systems available are presented followed by a mathematical analysis of the two types of systems.

2.2 EMI System Configuration

A typical Electromagnetic Induction (EMI) System consists of a transmitter coil, receiver coil, and the buried metallic object. The transmit coil when excited, radiates a primary magnetic field in the surrounding environment, which in accordance with Faraday's law, induces an emf in the buried object as well as the receiver coil.
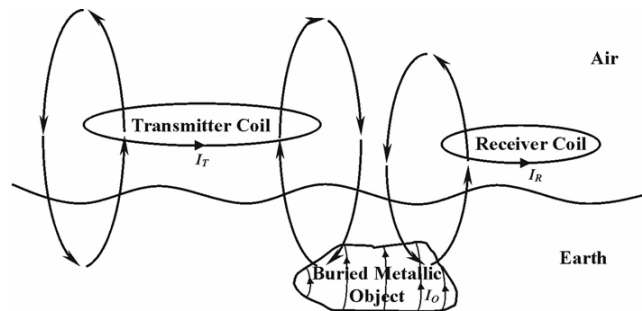
Figure 2.1 Schematic of a typical EMI system

This emf induced in the object generates eddy currents which radiate a secondary magnetic filed. The secondary magnetic field, in turn, induces a voltage in the receiver coil. Therefore, the total voltage induced in the receiver coil consists of two parts: the direct coupled voltage from the transmitter coil and the secondary voltage due to the object eddy currents. Figure 2.1 illustrates this basic concept.

EMI systems can be classified into one of two categories based on the type of excitation of the transmitter coil [7]. An EMI system which uses short duration current pulses to excite the transmitter coil is referred to as a pulsed EMI system. In one type of pulsed EMI system, the current pulses are increased to some maximum value and then turned-off abruptly. On the other hand a Continuous wave (CW) EMI system uses sinusoidal currents to excite the transmitter coil. Sinusoidal frequencies are in the range from below 1Hz to seldom higher than a few hundred kilohertz.

The choice of a pulsed or CW EMI system depends on many factors and the best method to use for discriminating UXO from clutter is a topic of considerable interest to the UXO community [8].

2.3 Circuit Model for a CW EMI System

Figure 2.2 shows the magnetically coupled circuit model of an EMI system, which is derived from the physical model of Figure 2.1. The transmit coil is represented by an equivalent self inductance and resistance, L_T and R_T respectively. Similarly the object can be represented by an inductance Lo and resistance Ro. This representation of the object is accurate only for a simple first order object such as a loop of thin copper wire (radius of the wire much less than the radius of the loop), and does not hold for more complex objects like the sphere and cylinder. Similar to the transmitter coils, the

inductance and resistance of the receiver coil are represented by L_R and R_R, respectively. Furthermore, the input impedance of the receiver amplifier is Z_R, the transmitter current is I_T, the object current is I_O, and the receiver current is I_R. The mutual coupling between the transmitter and the object, object and the receiver coil, and the transmitter and the receiver are denoted as M_{TO}, M_{OR}, and M_{TR}, respectively. The mutual coupling M_{TR} induces a voltage V_{DIRECT} at the receiver coil. It is desirable to reduce V_{DIRECT} as much as possible so that the output voltage is due to the object only. A figure-8 receiver coil also known as bucking coil can be used to minimize the direct coupling M_{TR} and therefore, the undesirable voltage $V_{DIRECT.}$
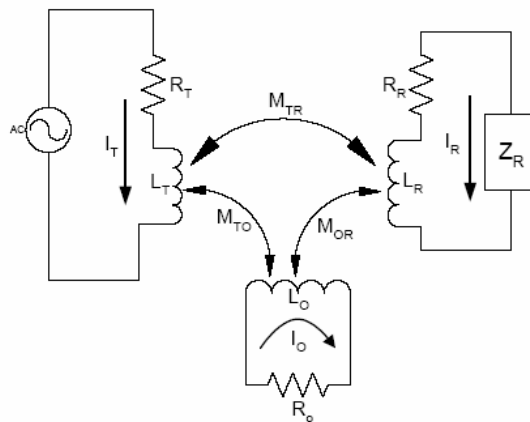
Figure 2.2 Magnetic Coupled Circuit used to represent a Continuous Wave (CW) Electromagnetic Induction Circuit

A figure-8 coil consists of two N-turn coils wound in opposite direction, connected in series such that flux passing through them will produce an equal but opposite voltage in each coil. Therefore, the net voltage across the coil pair will, theoretically, be zero.

6

Simple circuit theory can be used to derive a mathematical solution of the magnetically coupled circuit of Figure 2.2. The mathematical model allows one to define the fundamental operation of an EMI system. The receiver coil voltage in terms of the transmitter coil current can be obtained using Faraday's law of induction [5] and simple circuit theory.

Assuming sinusoidal excitation, the voltage V_1 induced in the object loop as a result of coupling between the object and the transmit coil is given by

$$V_1 = -j\omega M_{TO} I_T \tag{2.1}$$

The voltage V_{DIRECT} induced in the receiver coil due to the mutual coupling between the transmitter and the receiver coil is given by,

$$V_{DIRECT} = -M_{TR}\frac{d}{dt}I_T = -j\omega M_{TR}I_T \tag{2.2}$$

By Lenz's law a current I_O flows in the object loop and produces a secondary voltage in opposition to the induced voltage V_1 [9]. The voltage drop across the object loop V_{11} is given by

$$V_{11} = -(R_O + j\omega L_O)I_O \tag{2.3}$$

Assuming that Z_R is infinity (open circuit), and applying Kirchoff's voltage law, yields

$$V_1 + V_{11} = 0 \tag{2.4}$$

The expression for the object current can be obtained by substituting equations (2.2) & (2.3) into (2.4) and re-arranging terms, or

$$I_O = -\frac{j\omega M_{TO}}{R_O + j\omega L_O}I_T \tag{2.5}$$

7

The voltage V_{OBJECT} induced in the receiver circuit due to the object currents may be written as,

$$V_{OBJECT} = -j\omega M_{OR} I_O \qquad (2.6)$$

The response of the system to the object can be obtained by comparing the eddy current induced receiver voltage to the receiver voltage due to the primary field in the absence of the object, or,

$$\frac{V_{OBJECT}}{V_{DIRECT}} = -\frac{M_{TO}M_{OR}}{L_O M_{TR}} \frac{\alpha^2 + j\alpha}{1+\alpha^2} \qquad (2.7)$$

where $\alpha = \omega L_O / R_O$ is the response parameter of the system.

Mutual coupling between two circuits i and j, M_{ij}, can be represented in terms of the coupling coefficients of the two circuits k_{ij}, as

$$M_{ij} = k_{ij} \sqrt{L_i L_j} \qquad (2.8)$$

where L_i and L_j are the self inductances of circuits i and j respectively, and $|k_{ij}| \leq 1$

Using (2.8), equation (2.7) may be written as,

$$\frac{V_{OBJECT}}{V_{DIRECT}} = -\frac{k_{TO} k_{OR}}{k_{TR}} \frac{\alpha^2 + j\alpha}{1+\alpha^2} \qquad (2.9)$$

In (2.9), the term $(\alpha^2 + j\alpha)/(1+\alpha^2)$ known as the response function, depends only on the frequency and the electrical properties of the loop [10]. The term $k_{TO} k_{OR} / k_{TR}$ may be referred to as a coupling coefficient, the numerator, $k_{TO} k_{OR}$ is the coupling from the transmitter to the receiver through the object where as the denominator, k_{TR} is the direct coupling between transmitter and receiver. Coupling is independent of frequency

and only depends on the relative sizes, geometry, and the positions of the object with respect to the transmitter and receiver coils.

Figure 2.3 is a plot of the response function $(\alpha^2 + j\alpha)/(1+\alpha^2)$, with respect to the response parameter α. As α tends to zero, the real part of the response function tends to zero resulting in a purely imaginary response given by,

$$\frac{V_{OBJECT}}{V_{DIRECT}} = -\frac{j\omega L_O}{R_O} \frac{k_{TO} k_{OR}}{k_{TR}} \tag{2.10}$$

Equation (2.10) is referred to as the resistive limit. As α tends to infinity the imaginary part of the response function approaches zero and the real part asymptotically approaches unity. Under this condition, the response is given by

$$\frac{V_{OBJECT}}{V_{DIRECT}} = -\frac{k_{TO} k_{OR}}{k_{TR}} \tag{2.11}$$

which is referred to as the inductive limit. At the crossover frequency $\alpha = 1$ or $f_{crossover}$ $= R_O/2\pi L_0$, the real and imaginary parts of the response function are equal and the magnitude is approximately 3 dB below its asymptotic value. It should be noted that the general form of the response presented above is only valid for simple non permeable first order objects. (e.g. a thin copper loop of wire).

2.4 Circuit Model for a Time Domain EMI System

A time-domain (pulsed) EMI system differs from the CW EMI system only in the type of waveform used to excite the transmitter coil. Therefore, the magnetically coupled circuit model of Figure 2.2 can be used to model the pulsed EMI system. As the name suggests, in a pulsed EMI system, the transmitter coil may be excited by current pulses of short duration that increase to some maximum value and then abruptly fall to zero.
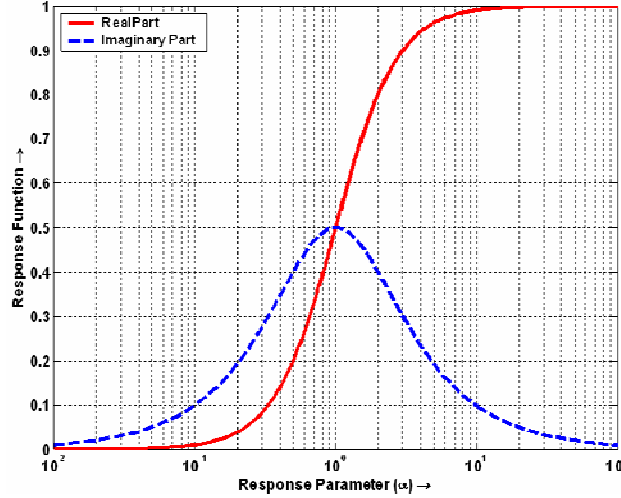
Figure 2.3 Frequency response of a simple first order target

For the pulsed EMI system a shunt resistance is connected across the transmit coil. This helps to ensure that the current turns off without oscillations or ringing.

The voltage induced in the object is proportional to the time rate of change of the transmitter current, so, generally speaking, it is desirable to turn off the transmitter current as rapidly as possible (without oscillations).

2.4.1 Coupling Between the Transmitter and Buried Object

A simple switched circuit model shown in Figure 2.4 can be used to illustrate the interaction between the transmitter current and the object current. In accordance with Faraday's Law of Induction [5], if a current I_T flows through the transmitter coil then the voltage induced in the object, V_{OBJ} is the product of the mutual coupling between the transmitter and the object, and the time rate of change of the transmitter current, or

$$V_{OBJECT} = -M_{TO} \frac{dI_T}{dt}$$

(2.12)

As illustrated in Figure 2.5 a transmitter current I_T is defined, which has an initial value, I_I, for all times t<0, and for times 0<t<T, linearly decreases until it is zero at t =T.

10

The voltage induced in the object is zero for time t<0, since the transmitter current $I_T(t)$ is constant during this time period. While the switch is in position A, the transmitter current decays linearly (0≤t≤T), and the voltage induced in the object is constant and is equal to $M_{TO}I_I/T$. During this period, the object eddy currents exponentially increase as shown in Figure 2.6. The object current, $I_O(t)$, when the switch is in position A can be written as,

$$I_O(t) = k_1 + k_2 e^{-t/\tau_o} \tag{2.13}$$

where $\tau_O = L_O/R_O$ is the time constant of the object.

At time t =0, the object current is zero and (2.13) yields $I_O(t=0) = k_1 + k_2$ or

$$k_1 = -k_2 \tag{2.14}$$

If the switch were left in position A indifinitely, the current would asymptotically approach V_{OBJECT}/R_O so

$$I_O(t=\infty) = \frac{V_{OBJECT}}{R_O} = k_1 \tag{2.15}$$

Using (2.14) and (2.15) in (2.13) yields,

$$I_O(t) = \frac{M_{TO}I_I}{TR_O}(1 - e^{-t/\tau_o}) \tag{2.16}$$

which is the charge up current of the object, valid only for $0 \le t \le T$.

The object current reaches a maximum value at time T, given by,

$$I_O(t=T) = \frac{M_{TO}I_I}{TR_O}(1 - e^{-T/\tau_o}) \tag{2.17}$$

At time t = T, the voltage induced in the object becomes zero, as the transmitter current no longer changes. Therefore, the peak object current in (2.17), starts to decay

11

exponentially toward zero, starting at time t = T. When the switch in Figure 2.4 is in position 'B' ($T \leq t \leq \infty$), the object current is given by,

$$I_O(t = T) = \frac{M_{TO}I_I}{TR_O}(1 - e^{-T/\tau_o})e^{-(t-T)/\tau_o}u(t - T)$$ (2.18)

where u(t) is the unit step function.
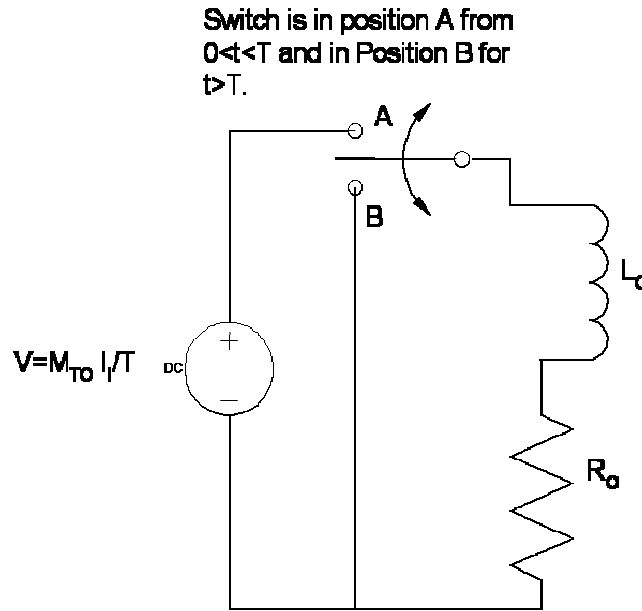
Figure 2.4 Circuit model describing the charge up and decay of object currents
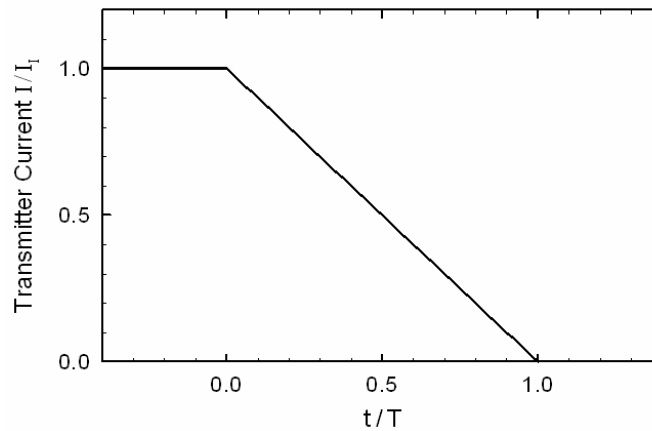
Figure 2.5 Normalized transmitter current versus normalized time

The exponential build up and the subsequent exponential decay of the object current is as shown in Figure 2.6.

The peak object current in (2.17) can also be expressed as,

$$I_O(\frac{T}{\tau_O}) = \frac{M_{TO}I_I}{L_O}\frac{(1-e^{-T/\tau_O})}{\frac{T}{\tau_O}} \qquad (2.19)$$

If $\frac{M_{TO}I_I}{L_O}$ is taken as a constant, then the peak object current at time t = T takes

the form,

$$y(x) = \frac{1-e^{-x}}{x} \qquad (2.20)$$

with $x = T/\tau_O$

The equation in (2.20), by L'Hopital's rule, is maximum when x=T/τ_O=0 or when the current shutoff time is much less than the time constant of the object, T<< τ_o.
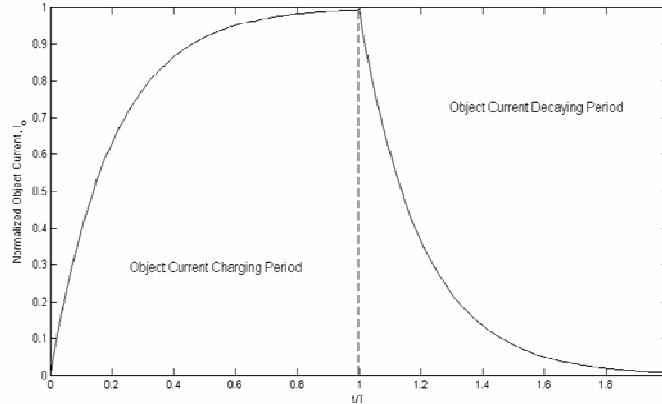
Figure 2.6 Object current versus time

Figure 2.7 shows a plot of the normalized peak current as a function of the ratio of turnoff time to the object time constant. From Figure 2.7, it is evident that the peak object current is maximum when x = 0 or when T<< τ_o or τ_o>>T.

13
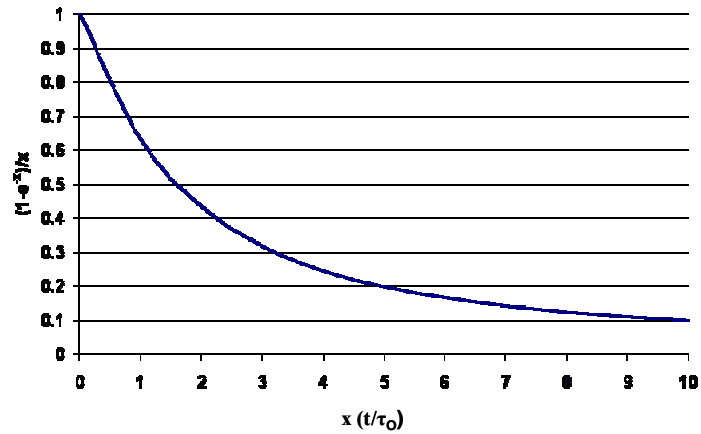
Figure 2.7 Normalized object current vs the ratio of shutoff time to object time constant.

Therefore, the turn off time of the transmitter current should be much less than the object time constant to maximize the object current.

This presents an interesting possibility in that the transmitter coil current turn off time T can be adjusted to supress the response of "small" objects with fast decay rates in favor of "large" objects with slow decay rates. This might be of value when one wishes to suppress the response form small surface clutter while simultaneously maintaining good sensitivity to larger, more deeply buried objects. Of course, the converse is not true, if the turn off time is fast enough to retain sensitivity to small objects then the system must also have good sensitivity to large objects.

2.4.2 Voltage at the Receiver- Open Circuit Case

The voltage at the receiver coil can be obtained in accordance with Faraday's Law, by simply differentiating the object current and multiplying by the mutual coupling between the object and the receiver coil, or

$$V_{OR} = M_{OR} \frac{dI_o(t)}{dt} \qquad (2.21)$$

14

If $T/\tau_o \ll 1$, then a Taylor series expansion of (2.16) provides a linear approximation, $\tilde{I}_o(t) = \dfrac{M_{TO}I_I}{TL_O}t$ for the object current during the time $0 \le t \le T$, which is shown in Figure 2.8 (b) as the dashed line.

Substituting $\tilde{I}_o(t)$ in (2.21) gives,

$$V_{OR}(t) = \frac{M_{OR}M_{TO}I_I}{L_oT}, \ 0{\le}t{\le}T \tag{2.22}$$

Similarly substituting (2.18) in (2.21) for $t \ge T$, gives

$$V_{OR}(t) = -\frac{M_{TO}M_{OR}I_I}{\tau_oTR_O}(1-e^{-T/\tau_o})e^{-(t-T)/\tau_o}, \ t{\ge}T \tag{2.23}$$

Using a Taylor series expansion in (2.23), the voltage induced in the receiver coil for t≥T can be written as

$$V_{OR}(t) = -\frac{M_{TO}M_{OR}I_I}{\tau_oL_o}e^{-t/\tau_o}, \ t{\ge}T \tag{2.24}$$

It is interesting to note that the ratio of the voltages in (2.22) and (2.24), is τ_o/T and since $\tau_o/T \gg 1$, the receiver voltage drops rapidly from the maximum value to the lower limit at t=T, and then the exponential decay starts, as shown in Figure 2.8 (c). This analysis agrees with the analysis given in [5]. There is also a direct coupled voltage at the receiver coil due to the coupling between the transmitter and receiver. The direct coupled voltage can be given as

$$V_{DIRECT} = -M_{TR}\frac{d}{dt}I_T(t) = \begin{cases} 0 & t < 0 \\ \dfrac{M_{TR}I_I}{T} & 0 \le t \le T \\ 0 & t > T \end{cases} \tag{2.25}$$

15
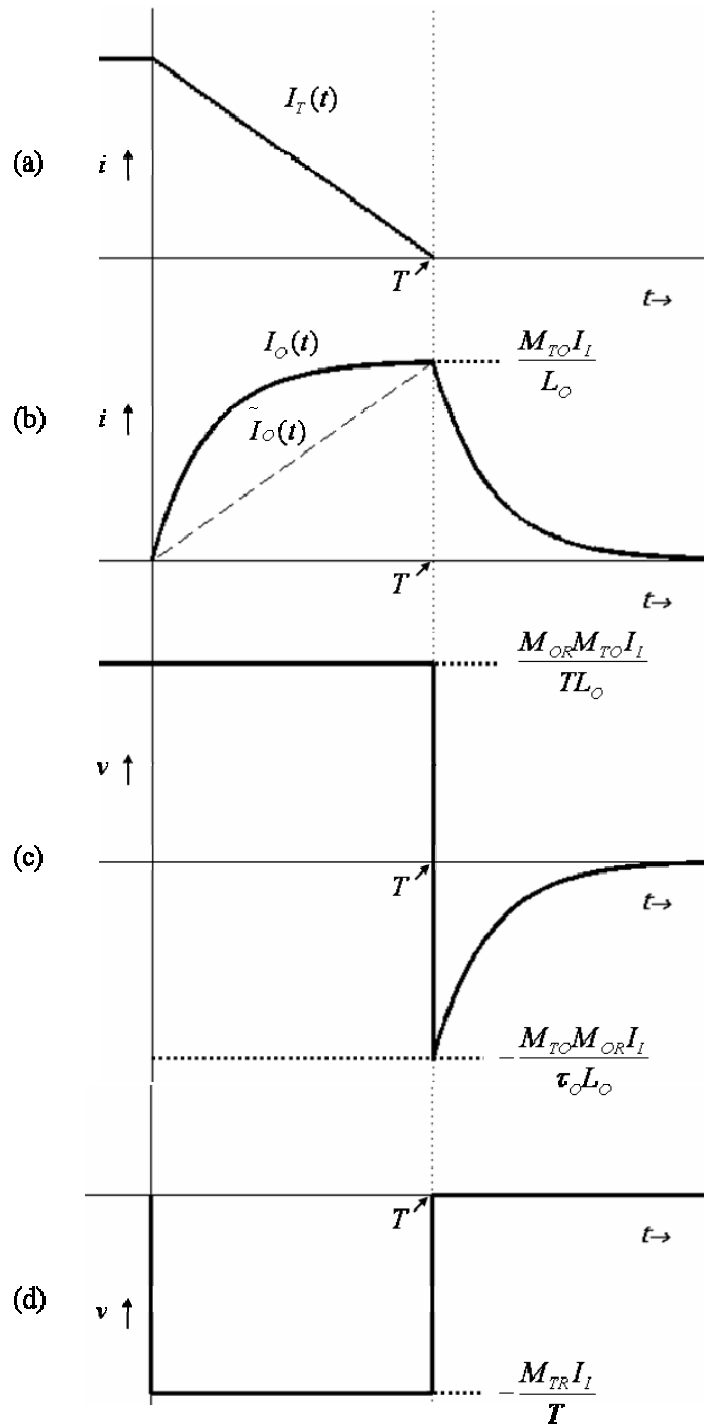
Figure 2.8 Representative plots for (a) Transmitter Current (b) Object Current (c) Object Coupled Receiver Voltage and (d) Direct Coupled Receiver Voltage. Dotted vertical line marks the time t=T.

16

The direct coupled receiver voltage is shown in Figure 2.8 (d). For the case of a bucking receiver coil, the transmitter coil couples equally and oppositely to each half of the receiver coil resulting in a zero net output voltage at the receiver when there is no object. If there is any imbalance between the two, however small, then there will be a component of the output voltage due to direct coupling.

If the residual coupling between the transmitter coil and the receiver coil is denoted as M_{TR}^{r} (where the superscript r represents residual) then

$$V_{\infty}^{r}(t) = \pm M_{TR}^{r} \frac{dI_{T}(t)}{dt} \tag{2.26}$$

The sign of the direct-coupled voltage depends upon the winding direction of the halves of the receiver coil with respect to that of the transmitter coil and upon which half has the larger direct coupling. Therefore it is possible for the direct-coupled voltage to either add or subtract from the object coupled receiver voltage for times $0 \leq t \leq T$.

2.5 Summary

An EMI system consists of three basic elements a transmitter coil, receiver coil, and the metallic object. In a CW EMI system, sinusoidal current is used to excite the transmitter coil with frequencies in the range from below 1Hz to seldom higher than a few hundred kilohertz. In a pulsed EMI system short current pulses flow through the transmitter coil and then turn off abruptly. In both the cases, the current in the transmitter coil radiates a field that induces a current in both the metallic object and the receiver coil. Additionally, the induced object-current radiates a secondary magnetic field which also induces a current in the receiver coil. If the receiver coil inductance is halved and the

transmitter coil is assumed to couple equally but oppositely to each half, then the net output voltage at the receiver due to direct coupling will be zero.

In the case of pulsed EMI system, it is beneficial to construct a transmitter current which is as large as possible before "turn off" but turns of rapidly without oscillations. A short current turn-off time generates a large object current. Furthermore, by controlling the current turn-off time, the response from objects that are not of interest like small metallic "clutter" can be suppressed in favor of objects of interest.

In the next chapter, the frequency domain transfer function obtained in section 2.3 is extended to take into account the physical characteristics of the transmitting coil, the receiver coil, and the receiver coil amplifier. Also, the design and development of EMI hardware based on the principles discussed in this chapter will be examined.

CHAPTER 3 HARDWARE DESIGN AND IMPLEMENTATION

In this chapter, first, the mathematical analysis of the frequency domain EMI system presented in the last chapter is extended to take into account the physical characteristics of the transmitter coil, receiver coil, and receiver coil amplifier. Next, a block diagram of a pulsed EMI system is presented, followed by a description of the electronics used to generate the transmitter current, and also the signal amplifier for the receiver coil. The final section in this chapter addresses the data acquisition hardware.

3.1 Transfer Function Characterization of the CW EMI System

Referring to the Figure 2-2 in chapter 2, the loop on the left represents the transmitter circuit (parameters subscripted with T), and the one on the right is the receiver circuit (parameters subscripted with R), while the middle loop represents the object to be detected (parameters subscripted with an O). The CW source drives a current I_T through the transmitter coil resistance and inductance R_T and L_T respectively. The coupling between the transmitter coil and object, object and receiver coil are denoted as M_{TO} and M_{OR} respectively. In general there is also a coupling between the transmitter and the receiver coil denoted as M_{TR}, but it can be kept to a minimum by using a figure-8 receiver coil, which is a pair of coils wound in a "bucking configuration". The object and receiver coil inductance and resistance pairs are respectively (L_O, R_O) and (L_R, R_R).

If the coupling between the circuits is weak then the object current may be written as [11],

19

$$I_O = \frac{j\omega M_{TO}}{R_O + j\omega L_O} I_T \tag{3.1}$$

Also, the transmitter current is just the source voltage divided by the impedance of the transmitter coil or

$$I_T = \frac{V_S}{(R_T + j\omega L_T)} \tag{3.2}$$

Substituting (3.2) into (3.1) yields

$$I_O = \frac{j\omega M_{TO} V_S}{(R_O + j\omega L_O)(R_T + j\omega L_T)} \tag{3.3}$$

The receiver current is the voltage induced in the receiver coil divided by the sum of the impedance of the receiver coil and the load impedance or

$$I_R = \frac{j\omega M_{OR} I_O}{Z_L + R_R + j\omega L_R} \tag{3.4}$$

which may be rewritten using (3.3) as

$$I_R = \frac{j\omega M_{OR} j\omega M_{TO} V_S}{(Z_L + R_R + j\omega L_R)(R_T + j\omega L_T)(R_R + j\omega L_R)} \tag{3.5}$$

The output voltage is obtained by the product of the receiver current and the load impedance as

$$V_{OUT} = \frac{Z_L j\omega M_{OR} j\omega M_{TO} V_S}{(Z_L + R_R + j\omega L_R)(R_T + j\omega L_T)(R_R + j\omega L_R)} \tag{3.6}$$

The frequency-dependent transfer function of the system V_{OUT}/V_S is given as

$$\frac{V_{OUT}}{V_S} = \frac{Z_L j\omega M_{OR} j\omega M_{TO}}{(Z_L + R_R + j\omega L_R)(R_T + j\omega L_T)(R_R + j\omega L_R)} \tag{3.7}$$

If we consider the case where the receiver coil is open circuited, the load impedance Z_L is infinite, then (3.7) would simplify to

$$\frac{V_{OUT}}{V_S} = \frac{j\omega M_{OR} j\omega M_{TO}}{(R_T + j\omega L_T)(R_R + j\omega L_R)} \qquad (3.8)$$

By defining the object and the transmitter coil break frequencies $\omega_O = R_O/L_O$ and $\omega_T = R_T/L_T$ respectively, (3.8) may be written as

$$\frac{V_{OUT}}{V_S} = \frac{M_{OR} M_{TO}}{L_T L_R} \frac{j\omega/\omega_T}{(1 + j\omega/\omega_T)} \frac{j\omega/\omega_O}{(1 + j\omega/\omega_O)} \qquad (3.9)$$

The frequency-dependent terms (rightmost two fractions) of (3.9) are high-pass filter terms, with break frequencies of ω_T and ω_O corresponding to the transmitter coil and the object respectively. Referring to Figure 3.1, as the operating frequency exceeds the break frequency, the response approaches unity and at the break frequency, the magnitude of the response is 0.707 or 3 dB below its high frequency asymptotic value. As the operating frequency approaches zero, the magnitude of the response decreases by 20 dB each time the frequency decreases by a factor of 10 (20 dB per decade roll-off). The phase of the high-pass filter starts out at 90 degrees well below the break frequency, is 45 degrees at the break frequency and approaches zero degrees well above the break frequency.

3.2 Optimal Number of Transmitter Coil Turns: Case 1 V_{OUT}/V_S Measurement

Theoretically the information regarding the object can be obtained by the measurement of the transfer function V_{OUT}/V_S given in (3.9). This would certainly be the case if the high-pass transmitter coil term in (3.9) were unity over all frequencies of interest. If the object frequency of interest is below the transmitter coil break frequency, then the response of the object would be attenuated by 20 dB each time the frequency

21

decreases by a factor of 10. For this reason, the transmitter coil break frequency should be somewhere near the lowest frequency of interest.
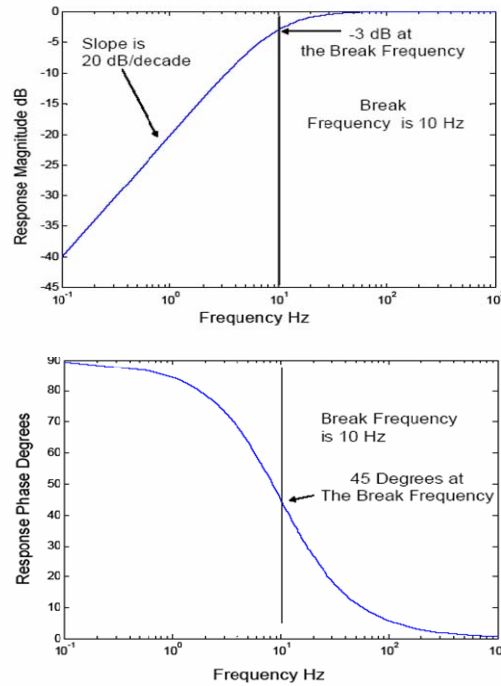
Figure 3.1 Transfer function characteristics of a high pass filter: (jf/10)/ (1+jf/10). Top figure is the magnitude response and bottom figure is the phase response.

The transmitter coil's break frequency is $\omega_T = R_T/L_T$ and R_T and L_T are proportional to N_T and N_T^2 respectively so that ω_T is inversely proportional to N_T where N_T is the number of turns of wire used to make the transmitter coil. So, the transmit coil should have enough turns to bring the transmit coil break frequency close to the lowest frequency of interest. But with the increase in the number of transmitter coil turns N_T, there is one more tradeoff that is probably important to consider. If we consider the object to be an N_O turn coil (q-coil), from (3.9), V_{OUT}/V_S, is proportional to $M_{OR}M_{TO}/L_TL_O$ and M_{OR} and M_{TO} are proportional to the product N_ON_R and N_TN_O respectively but L_T and L_O are proportional to N_T^2 and N_O^2 respectively so that $M_{OR}M_{TO}/L_TL_O$ is proportional to N_R/N_T (just the ratio of receiver to transmitter turns).

22

So, for a fixed number of receiver coil turns N_R, the amplitude of the response is inversely proportional to N_T. Therefore, there is a tradeoff between system voltage gain and system bandwidth. As N_T increases, the system bandwidth increases by lowering the transmitter coil break frequency but at the same time the overall gain of the system, N_R/N_T is also decreased.

3.3 Receiver coil and Receiver coil amplifier considerations for Case 1: V_{OUT}/V_S Measurement

The voltage induced in the receiver coil due to the eddy currents that flow on and within the object is usually small and therefore needs to be amplified. Generally, an operational amplifier is used to boost the weak signals induced into the receiver coil. In Figure 3.2, an operational amplifier connected in the non-inverting configuration is shown. It provides a voltage gain, $V_{out}/V_{in}=1+R_2/R_1$. The gain of the amplifier can be changed by adjusting the values of the resistors R_2 and R_1. The input impedance of the operational amplifier is very high, ideally infinite, but usually on the order of several mega ohms. Unfortunately, due to the high input impedance of the amplifier, a frequency is reached where significant currents will begin to flow in the parasitic coil capacitance, designated as C_R in Figure 3.2. A resonant circuit is formed by L_R, R_R and C_R of the receiver coil, due to which the input voltage V_{in} will increase proportionally with frequency at 20 dB/dec up-to the first self-resonance frequency of the receiver coil (which is around 10 kHz). This in-turn distorts the output voltage, which is no longer a faithful representation of the object response. The problems associated with the first self-resonance frequency of the receiver coils can be overcome by using a current-to-voltage converter [12], [13].
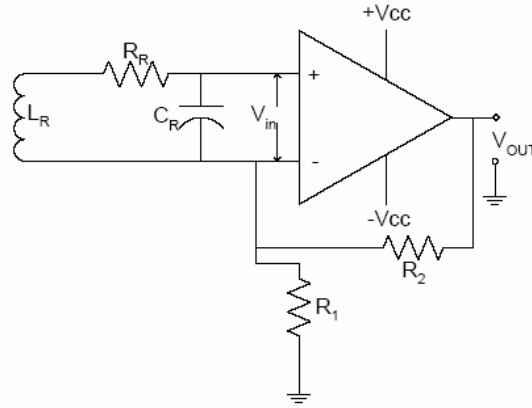
Figure 3.2 Operational amplifier connected in non-inverting configuration to the receiver coil. The parasitic capacitance of the receiver coil distorts measurements of the object's response.

3.4 Optimal Number of Transmit Coil Turns: Case 2 Object Current Measurement

The current flowing in the object due to the emf induced from the transmitter coil can be expressed in terms of the transmitter current, by re-arranging (3.1) as,

$$I_O = \frac{M_{TO}}{L_O} I_T \frac{j\omega/\omega_O}{1 + j\omega/\omega_O} \qquad (3.10)$$

The object response will not suffer distortion as long as the transmitter current I_T is frequency independent. But the transmitter current is given by (3.2) which may be written in terms of the transmit coil break frequency, $\omega_T = L_T/R_T$ as,

$$I_T = \frac{V_S/R_T}{1 + j\omega/\omega_T} \qquad (3.11)$$

For this case, since the transmitter current contains a low-pass filter term, the transmitter coil break frequency should be much higher than that of the object, $\omega_T \gg \omega_O$. Since ω_T is inversely proportional to the number of turns of the transmitter coil, N_T, the number of turns on the transmitter coil should be small. But, with fewer transmitter coil turns, N_T,

24

the coupling to the object will be low. So, there is a trade-off between bandwidth and coupling. More turns on the transmitter coil will lower the 3 dB break frequency, but a series resistance can be added to the transmitter coil to compensate for that. But, this can be done only if we increase the source voltage V_S or equivalently the source power.

3.5 Receiver coil and Receiver coil amplifier considerations for Case 2: Object Current Measurement

To eliminate the problems associated with the first resonance frequency of the receiver coil, a current-to-voltage converter is used as shown in Figure 3.3. It consists of an operational amplifier connected in an inverting configuration. The output voltage of the current-to-voltage converter is $V_{OUT}=-I_R R_F$, where I_R is the receiver coil current and R_F is the feedback resistance that sets the gain. The receiver coil current is nothing more than the voltage induced in the receiver coil divided by the impedance seen by the source.
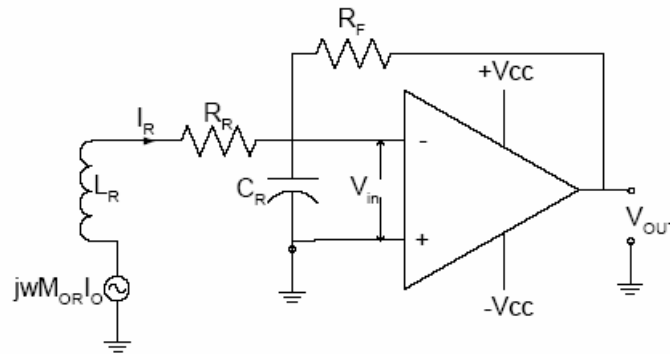
Figure 3.3 Operational amplifier connected in an inverting configuration as a current-to-voltage converter

Therefore, the output of the operational amplifier can be written as,

$$V_{OUT} = -\frac{R_F M_{OR}}{L_R}\left(\frac{j\omega/\omega_R}{1+ j\omega/\omega_R}\right)I_o \qquad (3.12)$$

25

where $\omega_R=R_R/L_R$ is the break frequency of the high-pass filter term in parenthesis. The break frequency of the high-pass filter term is inversely proportional to the number of turns on the receiver coil, N_R. Therefore, the break frequency can be set to lower value by increasing the number of turns. Figure 3.4 shows the plot of the break frequency of the receiver coil as a function of number of turns for a 1/3 m square figure-8 receiver coil using 18 AWG magnetic wire. From Figure 3.4, it can be seen that the break frequency decreases considerably with increase in the number of turns up to a certain point, after which it decreases but only slowly. Therefore, an optimum number of turns can be chosen to set the break frequency closer to the frequency of interest. There is an important difference between measuring the object current and measuring a voltage proportional to the object response.
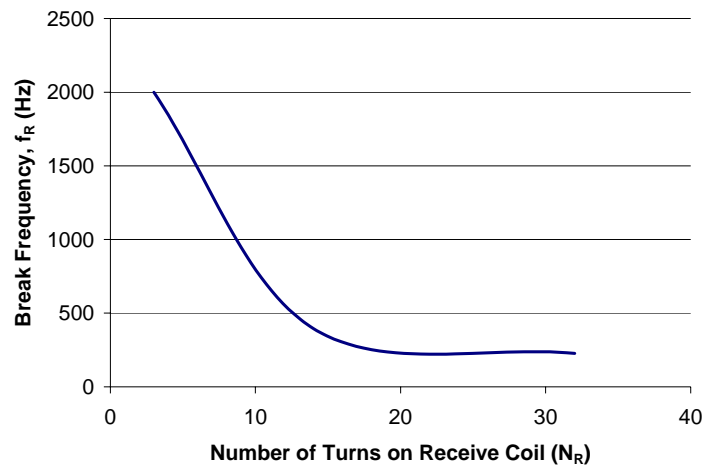
Figure 3.4 Plot of break frequency of the receiver coil as a function of number of turns

In the case of object current measurement using a current-to-voltage converter, the input resistance of the current-to-voltage converter is very low, so the parallel capacitance of the receiver coil is approximately short circuited at low frequencies. This causes the self-resonance of the receiver coil to shift to a much higher frequency for the

26

inverting op-amp configuration compared to that of the non-inverting op-amp configuration of Figure 3.3. As described in [13] it is even possible to compensate for the receiver coil roll-off below the break frequency, ω_R by replacing R_F in Figure 3.3 with the network shown in Figure 3.5. According to Prance et. al. [13] below the corner (3 dB) frequency, $f_{corner}=1/RC$, the gain of the current-to-voltage converter increases with a first order response (20 dB/decade) until the limit set by the bypass resistor RF is reached. This 20 dB/decade increase will exactly cancel the 20 dB/decade roll off below the receive coil break frequency ω_R. Also limiting the low frequency gain to a fixed value at DC serves to suppress amplifier drift.
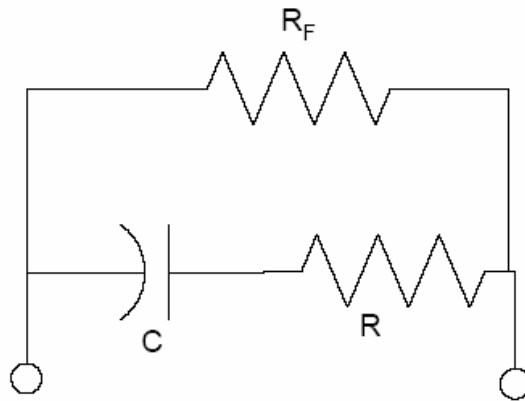
Figure 3.5 A modified feedback network that will extend the low frequency response of the current-to-voltage converter

3.6 Block Diagram of a Pulsed EMI System

A block diagram of a pulsed EMI system is shown in Figure 3.6. It consists of a square wave generator, which is used to "pulse" the voltage controlled switch. When the generated signal is "high", the switch closes and allows current I_T to flow through the transmitter coil for the duration of the pulse. When the pulse waveform falls below a characteristic "off" voltage the switch is opened. As discussed in the preceding chapter,

27

the transmit current must be allowed to reach a steady maximum value. Therefore, it is important that the duration of the pulse on-time is long enough for the transmitter current to reach a steady maximum value. It is also important that the off time of the current pulse is long enough to permit the receiver to capture the object's response which may be of significant amplitude for tens of milliseconds.

As stated earlier, flux from eddy currents that flow on and within the object produce a magnetic field that induces a voltage in the receiver coil. The receiver coil detects the object. The filtering and amplification section at the output of the receiver coil consists of a second order low pass filter, which converts the current in the receiver coil into voltage with some gain and also reduces, via low pass filtering, the high frequency noise.
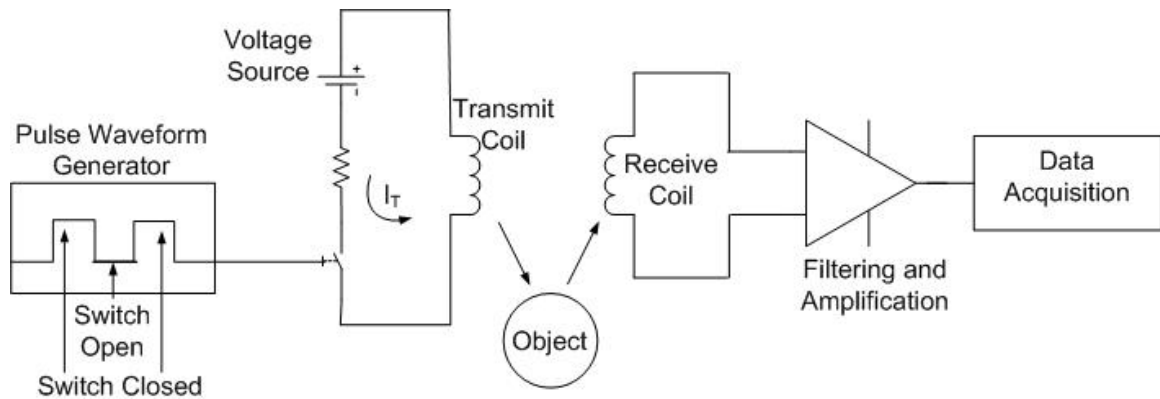
Figure 3.6 General block diagram of a pulse EMI system

Next the signal is passed to the Data Acquisition hardware, which is basically an Analog-to-Digital Converter (ADC). Different kinds of ADC's were used for data acquisition, and a brief description of each will be presented later in this chapter.

28

3.7 Transmit Current Generation

The circuit model for the transmitter section of the pulsed EMI system is shown in Figure 3.7. A PIC Microcontroller PIC16F88 is used to generate a pulse waveform with programmable period and duty cycle. The duration of the pulse is set to about 800 μs with a repetition frequency of 50 Hz. The microcontroller provides a TTL output, which is fed to a MOSFET/IGBT driver chip IXDN404PI from IXYS Corp. which boosts the TTL signal from the microcontroller to a +12 V output signal. The MOSFET driver IC has low output impedance, which is essential for a faster turn off of the IGBT [14]. An Insulated Gate Bipolar Transistor (IGBT) IRG4PH40K from International Rectifiers Inc. is used as the switch in the transmitter current generation circuit. The output of the driver is connected to the gate of the IGBT through a resistor R_Series.
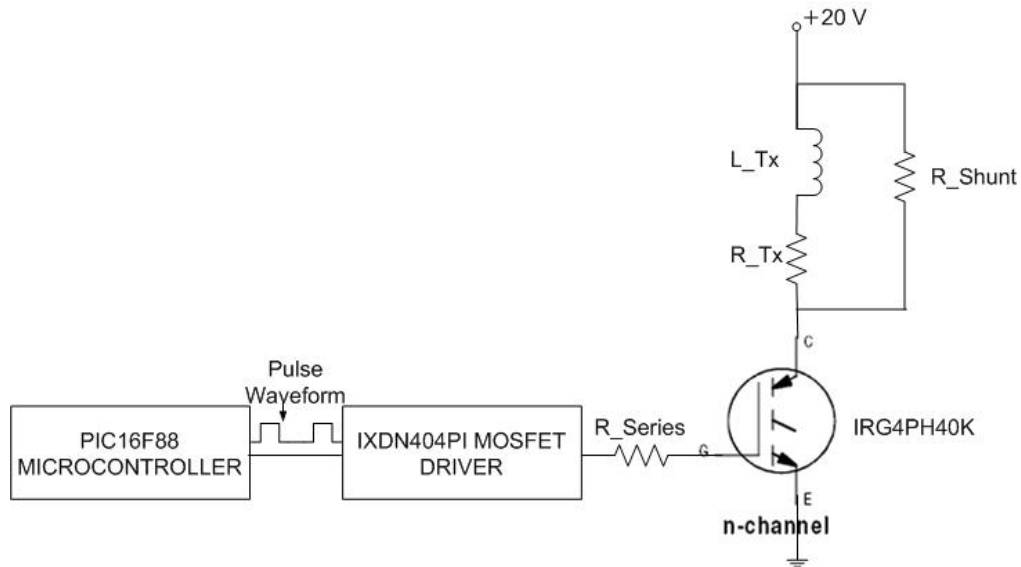
Figure 3.7 Circuit Schematic for the Transmitter

This resistor along with the output impedance of the MOSFET driver and the intrinsic internal gate capacitance of the IGBT controls the turn on and turn off times of the IGBT [14].

29
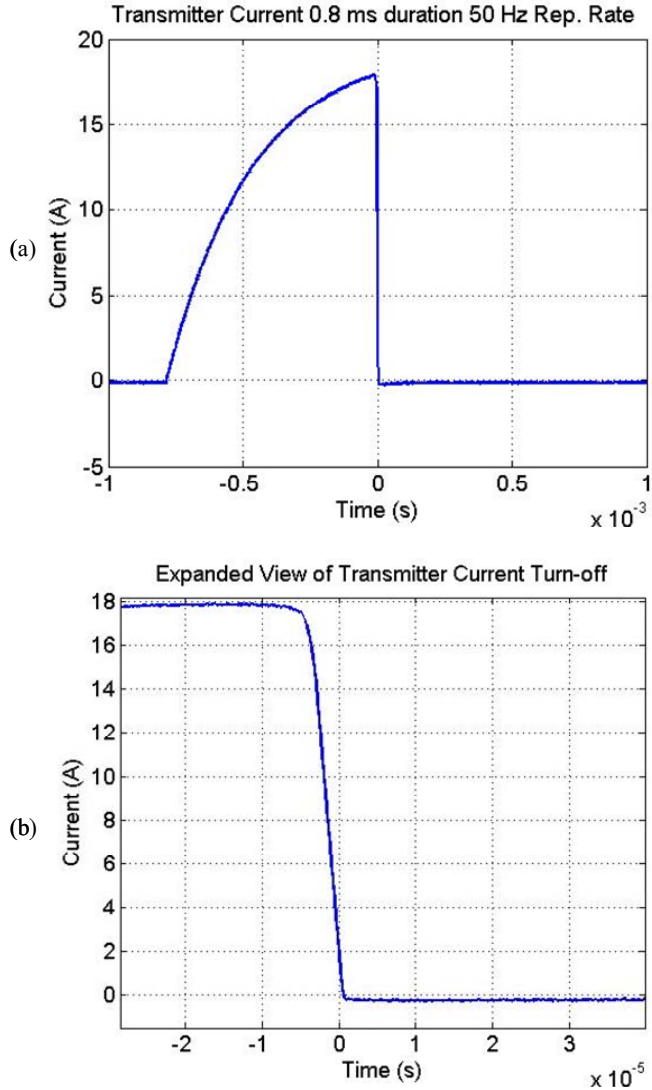
Figure 3.8 (a) Transmit current pulse 800μs duration, 50Hz repetition rate. (b) The current turn-off time is approximately 5 μs.

The shunt resistor R_Shunt across the transmitter coil in Figure 3.7 is used to dampen the oscillations in the transmitter current. As shown in Figure 3.8 (a), when the IGBT is on, the transmitter current exponentially increases to a maximum value of approximately 18A. The maximum current value was determined by the choice of a 24V power supply.

When the IGBT turns off, the current falls to zero in approximately 5µs, as shown

in Figure 3.8 (b).
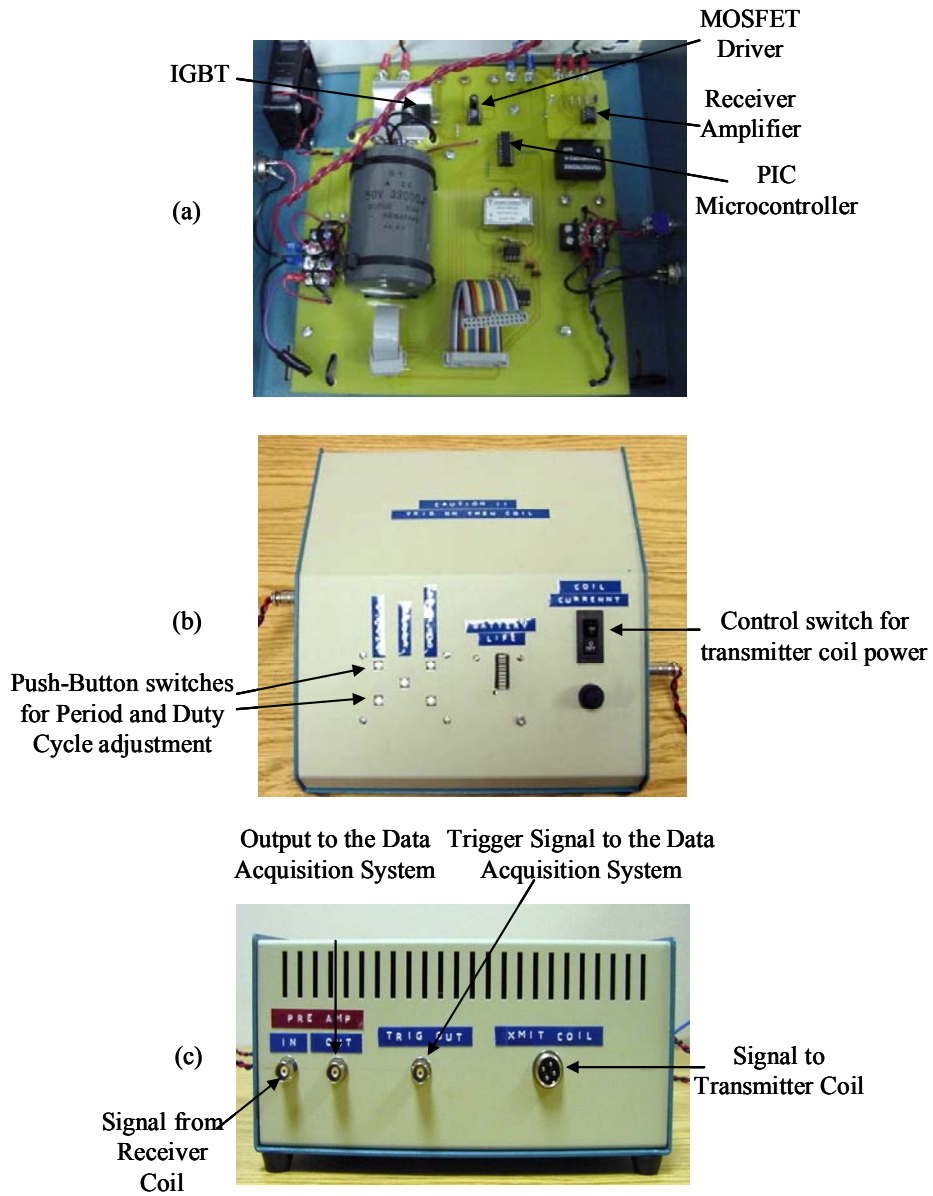
Figure 3.9 (a) Components of the pulser on a printed circuit board, (b) Front end of the
pulser box, (c) Back end of the pulser box

Figure 3.9 shows the components of the system packaged into a portable unit, referred to

as the "pulser". External connectors are provided for the 24V and 12V power supplies

and for the transmit coil. Another connector provides access to the IGBT gate signal which is used as the trigger signal for Data Acquisition. A safety switch that interrupts the power supply to the coil, and the push button switches for adjusting the period and duty cycle of the pulse, are all mounted on the front of the box.

3.8 Transmitter and Receiver Coil Construction

Taking into account the design considerations discussed in the earlier sections, a 1m×1m square transmitter coil was constructed with 18 AWG magnetic wire wound around a wooden frame. In general, the field strength at the center of the coil is inversely proportional to the radius of the coil, and the field strength along the axis of the coil
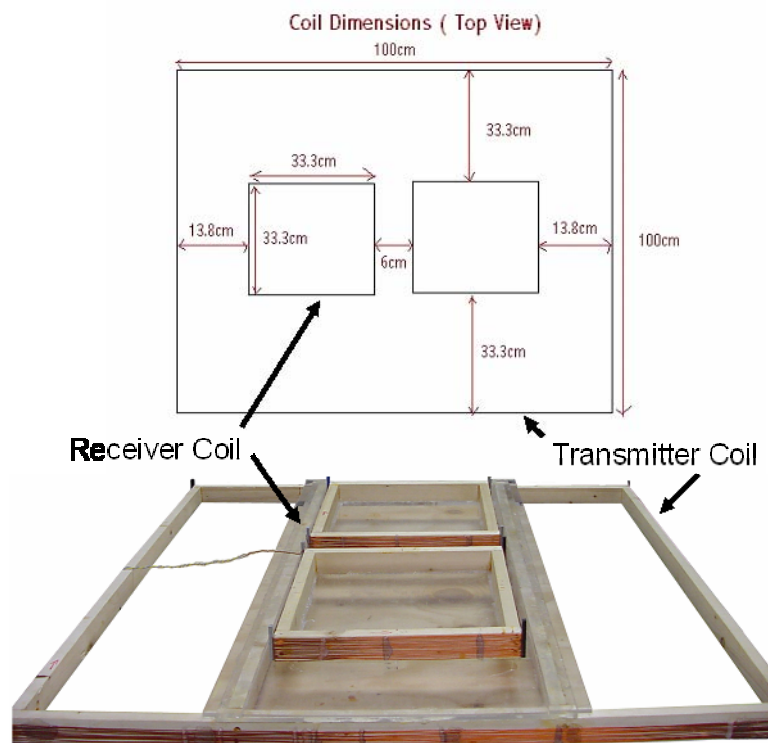
Figure 3.10 Square transmitter and rectangular "figure 8" receiver coil. The transmitter coil consist of 10 turns, R=917 mΩ, L=357 μH (measured at 1 kHz). The receiver coil consist of 14 turns per coil, total R=832 mΩ, L=335 μH (measured at 1 kHz.). Spacing between turns on both transmitter and receiver coils is approximately 0.06".

decreases faster as the radius of the coil decreases. A "rule of thumb" that takes into account these opposite trends states that a coil sees a target approximately one coil diameter deep. UXO targets buried deeper than 1m are usually not considered dangerous and so a square coil of 1m diameter was considered to be appropriate for this application.

Figure 3.10 shows a diagram of the coils with dimensions marked, along with the final product and relevant electrical characteristics. A "figure 8" shape (sometimes referred to as a bucking configuration) was chosen for the receive coil. As explained earlier, each loop of the figure eight configuration, couples equally but oppositely to the transmitter coil producing zero output in the absence of a target. As shown in Figure 3.10, the receive coils were fixed to a plexiglas sheet which rests on a larger thicker sheet. Guides were placed on either side of the receive coil sheet allowing the receiver coil to slide only along one axis. The plexiglas sheet holding the receiver coils is adjusted while monitoring the receiver coil voltage on an oscilloscope. The receiver coils are fixed at the position that produces a minimum voltage.

3.9 Receiver signal Conditioning

For the work presented in this thesis, a second order low pass filter designed using an operational amplifier in the inverting configuration is used as the receiver signal conditioning circuit. The schematic of the filter is shown in Figure 3.11. Since there is very little target information at higher frequencies, the cut-off frequency of the filter was set to 10 kHz, and the gain was set to 20 dB. The receiver amplifier shown in Figure 3.11 was simulated in Pspice to determine its frequency response characteristics. The frequency response of the designed practical circuit was obtained using an HP89410A

Vector Signal Analyzer. The frequency response plots of the filter are shown in Figure

3.12 and Figure 3.13 respectively.
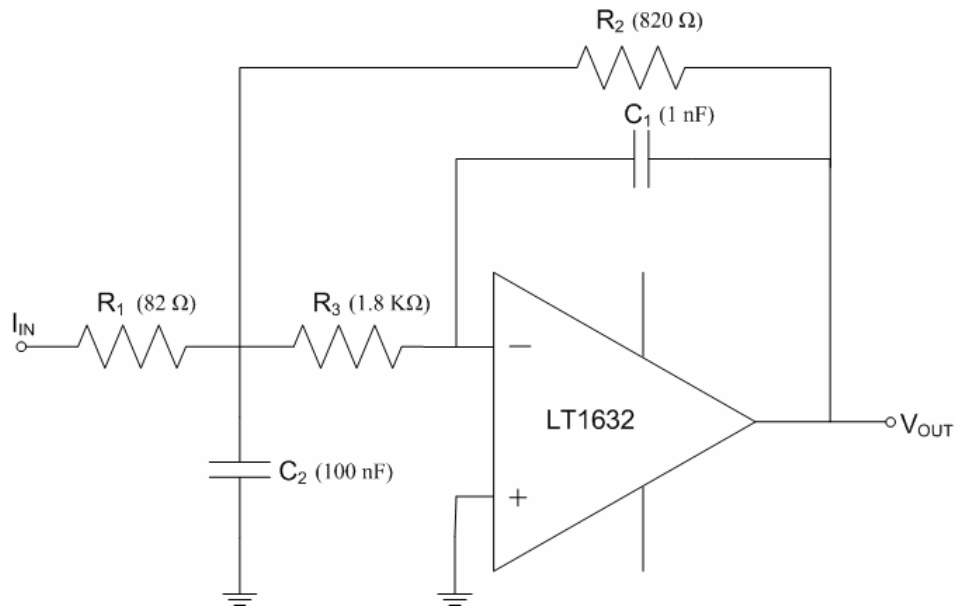
Figure 3.11 Schematic of the Receiver Amplifier
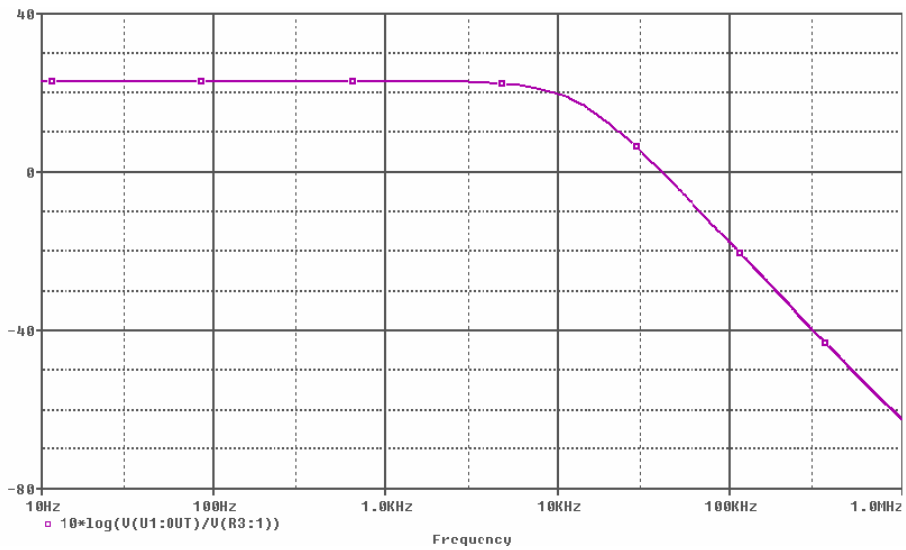
Figure 3.12 Frequency Response plot of the Receiver Amplifier from Pspice
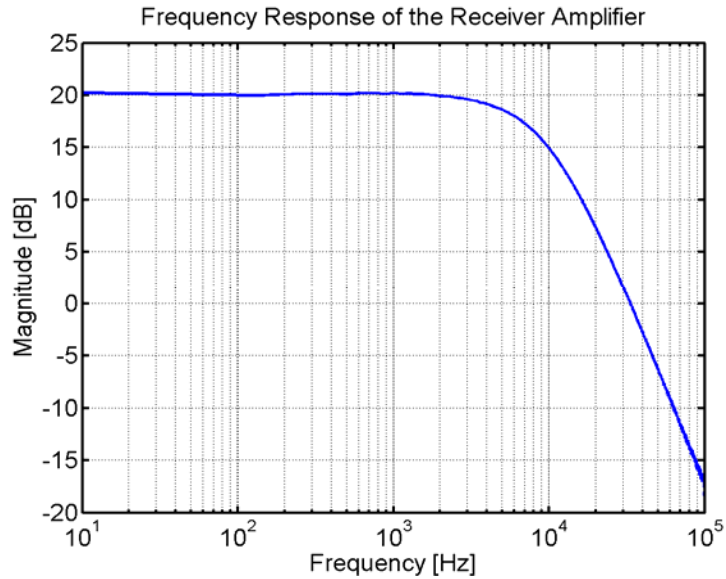
Figure 3.13 Frequency Response plot of the Receiver Amplifier measured using an HP89410A Vector Signal Analyzer

The receiver amplifier circuit shown in Figure 3.11 has some drawbacks. The input impedance looking into the inverting input of the amplifier is nothing but the resistor R1. This resistor is in series with the receiver coil, and adds to the resistance of the receiver coil. The additional resistance causes the break frequency of the high pass filter term in the receiver coil response to shift upwards, which reduces the bandwidth of the system. As discussed earlier, a current-to-voltage converter has very low input impedance and does not affect the low frequency cut-off of the receiver coil.

3.10 Data Acquisition

The output voltage of the receiver coil amplifier for different targets was fed to an analog-to-digital converter (ADC) for data logging and analysis purposes. Table 3.1 presents the different data acquisition devices that were investigated and presents a comparison of parameters such as sampling rate, resolution, and range of the ADC's.

Table 3.1 Comparison of Data acquisition devices

Name of ADC	Sampling Rate	Resolution	Range	Remarks
Compuscope (CS) 1602 from Gage Applied Inc.	100kS/s-2.5 MS/s	16-bit	±500 mV -±10 V	Plugs into the PCI slot of a desktop computer.
DAQcard-6062E from National Instruments	500 kS/s	12-bit	±50 mV - ±10 V	Plugs into the PCMCIA slot of a Laptop computer.
ADC-216 from PICO Technologies	333 kS/s	16-bit	±10 mV - ±20 V	Plugs into the parallel port of a PC.
cRIO with cRIO-9215 from National Instruments	100 kS/s	16-bit	±10 V	Plugs into the Ethernet port of a PC.

The CS1602 is a 16-bit ADC which is installed on a desktop computer as it is a PCI bus card. It has 2 differential analog inputs, an external trigger and clock inputs. The *GageScope* data acquisition software helps in displaying and storing the data acquired by CS1602. It provides control of the sampling rate, input range, and trigger level.

The DAQcard-6062E is a 12-bit ADC which can be installed in the PCMCIA slot of a laptop. It has 16 analog inputs, 2 analog outputs, and 8 digital I/O lines. *LabVIEW* software from National Instruments can be used to store the data acquired using the DAQ card.

The ADC216 is a 16-bit data acquisition device, which can be plugged into the parallel port of a desktop or a laptop. It has 2 analog inputs, and an external trigger input. *Picoscope* software from PICO technologies can be used to program the device.

36

Compact Reconfigurable I/O (cRIO) is a real-time embedded controller from National Instruments. It has a 200 MHz Pentium class processor that reliably and deterministically executes the *LabVIEW* Real-Time applications. It has a reconfigurable embedded chasis, which contains the reconfigurable I/O (RIO) Field Programmable Gate Array (FPGA) core. The RIO core is connected to the cRIO embedded real-time controller through a local PCI bus interface. It comes with many different types of I/O modules for data acquisition and storage. It connects to a computer through either an RS-232 serial port or an Ethernet port. The information provided in Table 3.1 for the cRIO is for one of the I/O modules, cRIO-9215, which is an analog input module. The Compuscope1602 card with Gagescope software was used for laboratory as well as stationary field measurements. For field measurements which required mobility, the DAQcard-6062E was used as the data acquisition device. These measurements are discussed in detail in the next chapter. The complete EMI system is shown in Figure 3.14.
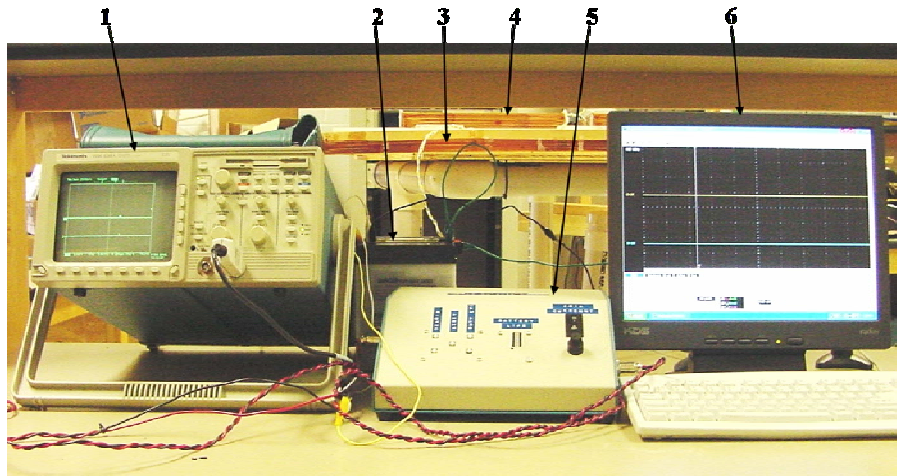
Figure 3.14 Photo of pulse EMI System. (1) Tektronix Oscilloscope (2) Battery power supply for the "pulser" (3) Transmitter coil (4) receiver coil (5) Pulser and (6) Gagescope PC

3.11 Summary

The pulse system consists of four major parts; the pulser, sensor coils, signal conditioning, and finally the data acquisition hardware. The pulser was built into a portable unit, capable of switching a 18 A (peak) transmit current "off" in approximately 5µs. Care was taken in the construction of the sensor coils, with concentrated efforts to eliminate parasitic capacitance, obtain precise symmetry to reduce direct coupling between transmitter and receiver coils, and build the coils large enough to detect large metallic objects at expected UXO target depths. Low-pass filtering and amplification of the response at the receiver coil increased SNR by rejecting responses not of interest and by amplifying the desired signal. After low-pass filtering and amplification (signal conditioning), the analog signal is converted to digital form and stored using the data acquisition hardware and the accompanying software.

In the next chapter, first, the data collected in the laboratory for a variety of targets is examined and compared with the analytical data in an effort to quantify the performance of the pulse EMI system. Next, data collected at the Naval research Laboratory's (NRL) Blossom Point test site is analyzed to examine the detection and discrimination capabilities of the pulse EMI sensor system.

CHAPTER 4   PULSED EMI MEASUREMENTS

In this chapter the laboratory measurements obtained from the pulsed EMI system for targets such as copper loops, and UXO-like cylindrical targets are compared with the analytical response in an effort to quantify the performance of the system. Next, the field measurements taken at the Blossom Point Test Site, in Maryland are analyzed to demonstrate the detection and discrimination capability of the pulsed EMI sensor.

4.1 Laboratory Measurements

As mentioned before, the purpose of the laboratory measurements was to ensure that the pulsed EMI system is working properly. Specifically, the measured response of test targets is compared with their analytically derived counterpart and to the response obtained from finite element modeling (FEM) [7]. The first target chosen for comparison purposes was the wire loop (sometimes referred to as a q-coil). As shown in Figure 4-1, the q-coil consists of a wire of thickness a, and loop radius b, constructed such that $a<<b$.

Figure 4.1 Example of a q-coil (5 inch copper loop with 18 AWG copper wire)

39

Referring to (2.25), for time $t>T$, the receiver coil voltage takes the form of a simple exponential decay or

$$V_{OR}(t) = -Ke^{-t/\tau_o} \qquad (4.1)$$

where K is a constant and the object time constant is given by, $\tau_O = L_O/R_O$. The object inductance is given by

$$L_O = \mu b \left[\ln\left(\frac{8b}{a}\right) - 1.75 \right] \qquad (4.2)$$

where a is the wire radius, b the mean loop radius, and μ is the effective permeability of the wire [1].

The resistance of the object is given by,

$$R_O = \frac{L}{\sigma A} \qquad (4.3)$$

with L the wire length, A its cross-sectional area, and σ is the conductivity of the wire [2].
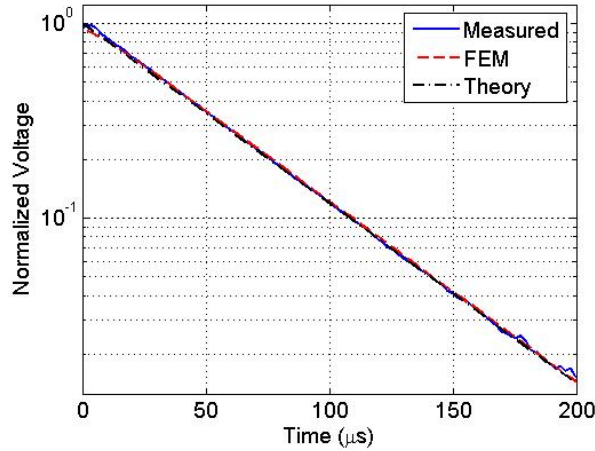
Figure 4.2 Theoretical, FEM, and Measured Time Domain response of 18 AWG 5" copper loop

L, a, and b were measured with a micrometer for precise calculation of the time constant of the loop. The accuracy of the EMI system was evaluated by comparing the three

40

decay rates obtained from calculation, measurement, and FEM modeling. Figure 4-2 shows a plot of the time response of the copper loop obtained from calculations, FEM modeling, and measurements. It can be seen from the figure that the agreement among the three responses is excellent. The next targets used to validate the performance of the pulsed EMI system are the UXO like cylinders. The cylinders are categorized into four series based on the dimensions and each series is further subdivided into three types based on cylinder wall thickness. The wall thickness plays an important part in discrimination. Solid cylinders and cylinders with ½" wall thickness are used to model ordnance while cylinders with ¼" wall thickness might be representative of clutter. The cylinder test target set is shown in Figure 4-3 and their dimensions are given in Table 4.1.

Figure 4.3 UXO test objects consisting of 12 cylinders outlined in Table 4.1

Figure 4.4 shows the measured time domain response of the "2 series" (3" diameter × 12" height) cylinders with same diameter and height but different wall thicknesses. The response has a steep slope in the early time and a gradual slope later. The early time response corresponds to higher frequencies that do not penetrate the object.

Table 4.1 Physical properties of UXO test objects. Length (L), diameter (D), and wall thickness.

Steel Cylinders			
Target	Wall Thickness (in)	L (in)	D (in)
1A	0.25	8	2
1B	0.5	8	2
1C	solid	8	2
2A	0.25	12	3
2B	0.5	12	3
2C	solid	12	3
3A	0.25	16	4
3B	0.5	16	4
3C	solid	16	4
4A	0.25	24	6
4B	0.5	24	6
4C	solid	24	6

Therefore, not surprisingly, the responses of the three cylinders are almost identical in early time. As the fields penetrate deeper into the object at late time (low frequencies), the response of the otherwise visually identical targets should be different. However, it is very difficult to measure the late time response as the signal is overwhelmed by noise in late time. Hence, measured data only out to 17 ms is shown in Figure 4.4. In order to better understand the nature of the response beyond 17 ms, the FEM responses [7] of the cylinders out to 40 ms are compared in Figure 4.5.
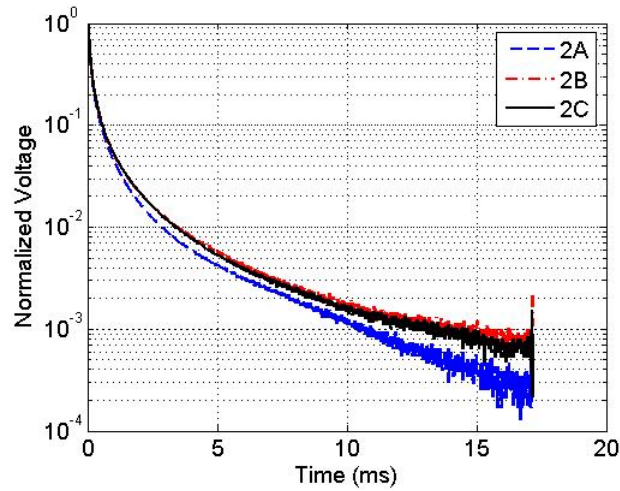
Figure 4.4 Measured decays for "2 series" cylinders identical except for wall thickness
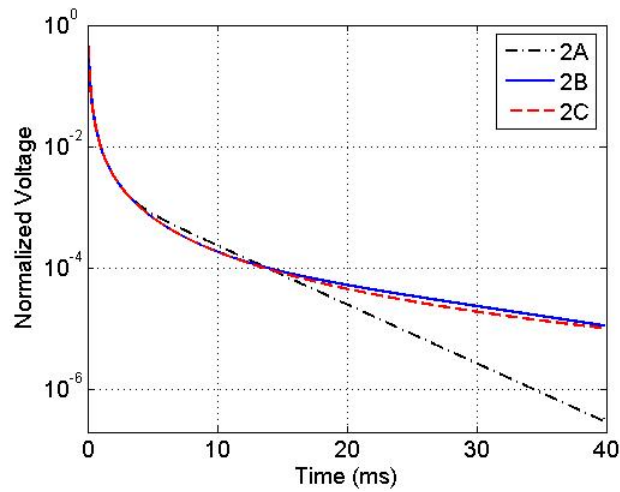
Figure 4.5 FEM decays for "2 series" cylinders identical except for wall thickness

From Figure 4.5 it is observed that there is a clear difference in the decay behavior depending on the wall thickness. The response of cylinder 2A decays faster and has a pure exponential decay starting at about 5 ms. Whereas cylinder 2B goes into the pure exponential regime at around 20 ms and the exponential portion of the response for cylinder 2C would have been noticeable, if the response was extended beyond 40 ms. So,

it is very important to obtain the late time response of the targets to be able to discriminate among different targets.

4.2 Field Measurements

The purpose of visiting the Blossom Point test site in Maryland was to demonstrate the detection and discrimination capabilities of the pulsed EMI sensor. The tests were done in August 2005, for a period of 4 days. Two types of tests were carried out at the test site. The first one was a stationary test or Pit test of the EMI sensor which was carried out on a platform over a pit. The second type is a dynamic test where the EMI sensor is mounted on a flat fiberglass trailer and pulled by a truck down a lane. APPENDIX A gives the details of the two types of tests. In the following sections of this chapter, results obtained from the two tests are presented.

4.2.1 Pit Measurements

Section A.1 of APPENDIX A gives the details of the setup for the pit test. Figure 4.6 shows some of the targets used in the pit test.

Figure 4.6 Targets used in Pit test

The responses of different targets were obtained for different target depths, and also different target positions with respect to the center of the transmitter and receiver coils.

44

4.2.1.1 Response of 4 inch Carbon Steel Sphere

The first target measured in the pit testing is a 4 inch carbon steel sphere. The details of the tests carried out for the 4 inch carbon steel sphere are given in Table A.1. Figure 4.7 shows a photograph of the 4 inch Carbon Steel Sphere. Figure 4.8 presents data in File1 from Test1 in Table A.1, when the coils are far away from the sphere. This data can be referred to as background response since the target is so far away from the coils.

Figure 4.7 Picture of the 4 inch Carbon Steel Sphere from the Pit testing
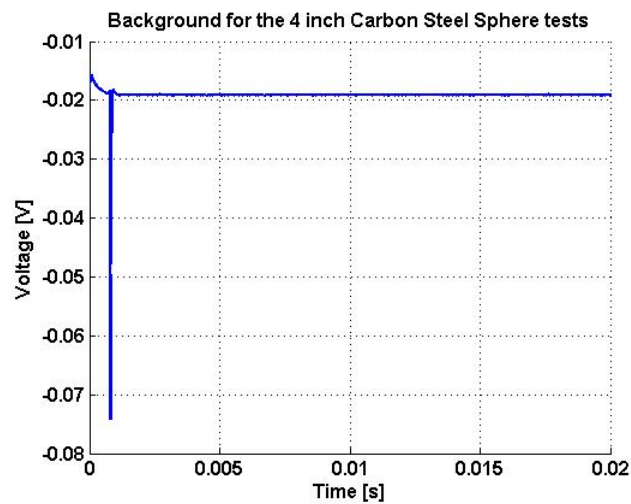
Figure 4.8 Background Response for the sphere tests

Figure 4.9 shows the data of File 8 from Test1 for the carbon steel sphere with background subtraction. Figure 4.10 shows the zoomed in data indicated by the dotted box in Figure 4.9.

From these plots it can be observed that when the coils are far away from the target, there is no exponential decay observed, and when the coils move closer to the target, the long tail of the exponential decay becomes evident.
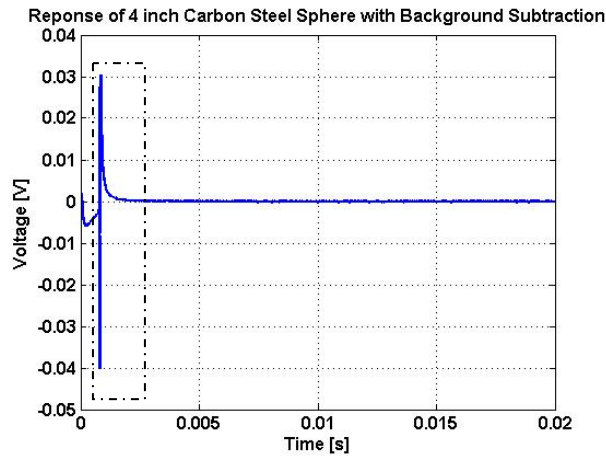
Figure 4.9 Response of 4 inch carbon steel sphere with background subtraction. Sphere is relatively close to the transmitter and receiver coils
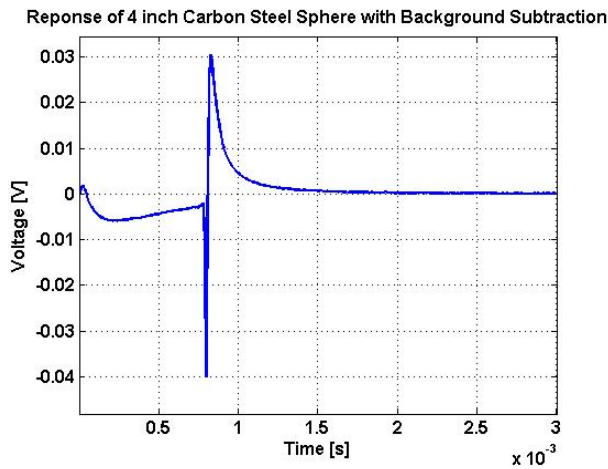
Figure 4.10 "Zoomed-in" response of 4 inch carbon steel sphere with background subtraction

46

4.2.1.2 Response of the 105 mm shell

The next target measured was the 105 mm shell. For the 105 mm shell different measurements were taken with horizontal and vertical orientations of the target with respect to the axis of the coils, as well as different target depths and locations with respect to the center of the coils. Table A.2 summarizes the data acquired for the 105 mm shell. Figure 4.11 shows a plot of the response of the 105 mm shell with background subtraction. The response shown is of File12 from Test1, with the incident magnetic field in the transverse direction with respect to the axis of the target. Figure 4.12 shows the response corresponding to data files 11 and 12 with background subtraction from Test1, and the data is zoomed in to look at the exponential decay of the target. For the data presented here, the number of data averages was set to 25.
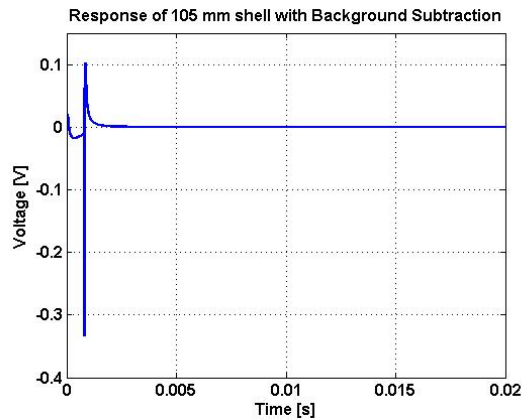
Figure 4.11 Response of 105 mm shell with background subtraction
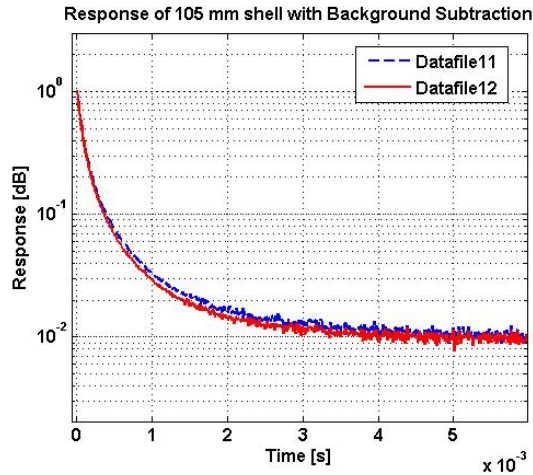
Figure 4.12 "Zoomed-in Response" of 105 mm shell with background subtraction as a function of position

4.2.1.3 Response of 81 mm mortar

The next target tested was an 81 mm mortar. For the 81 mm mortar, measurements were taken with horizontal and vertical orientations of the target with respect to the axis of the coils. Table A.3 summarizes the data acquired for the 81 mm mortar. For the data acquired for the 81 mm mortar, 25 data averages were taken. Figure 4.13 shows the data of File 7 with background subtraction for the 81 mm mortar with the incident magnetic field along the axis of the target.
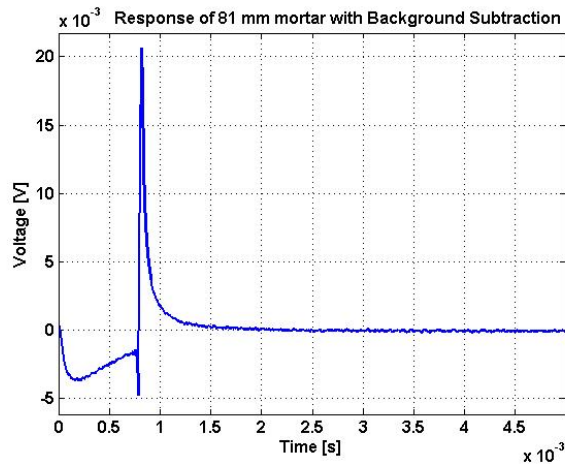
Figure 4.13 "Zoomed-in" response of 81 mm mortar with background subtraction

48

4.2.1.4 Response of 40 mm shell

The next target tested was a 40 mm shell. For the 40 mm shell, measurements were taken with horizontal and vertical orientations of the target with respect to the axis of the coils. For the data acquired for the 40 mm shell, 25 data averages were taken. Table A.4 summarizes the data acquired for the 40 mm shell. Figure 4.14 shows the data of File 7 with background subtraction for the 40 mm shell with the incident magnetic field along the axis of the target.
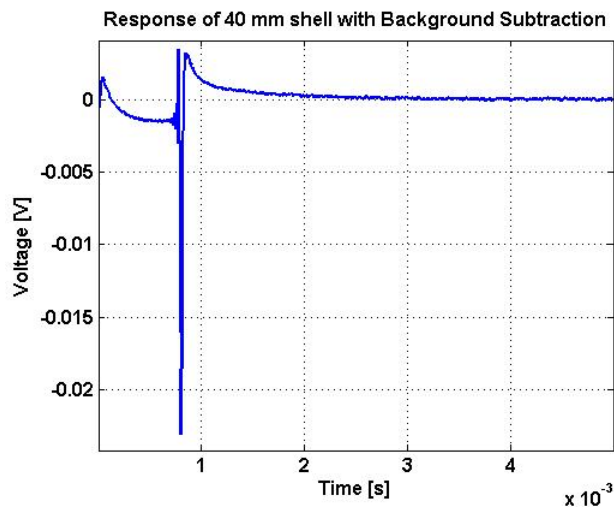
Figure 4.14 "Zoomed-in" response of 40 mm shell with background subtraction

4.2.1.5 Response of Cylinder E

The next target tested was Cylinder E. For the Cylinder E, measurements were taken with horizontal and vertical orientations of the target with respect to the axis of the coils. For each orientation measurements were taken for two different target depths with respect to the coils. Figure 4.15 shows a picture of cylinder E along with a schematic showing the height of the cylinder from the receiver coil for Test1.
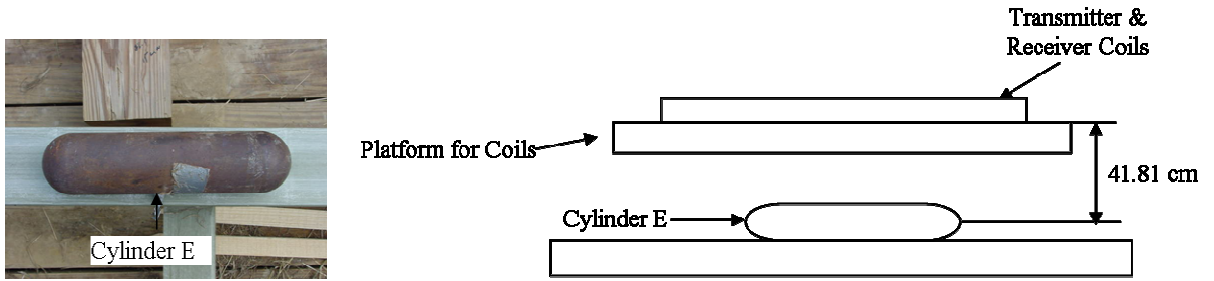
Figure 4.15 Depth of Cylinder E with respect to the top of the Platform for Test1

Table A.5 summarizes the data acquired for Cylinder E. For the data acquired for Cylinder E, 50 data averages were taken. Figure 4.16 shows the data of File 11 from Test 4 with background subtraction for Cylinder E with the incident magnetic field along the axis of the target.
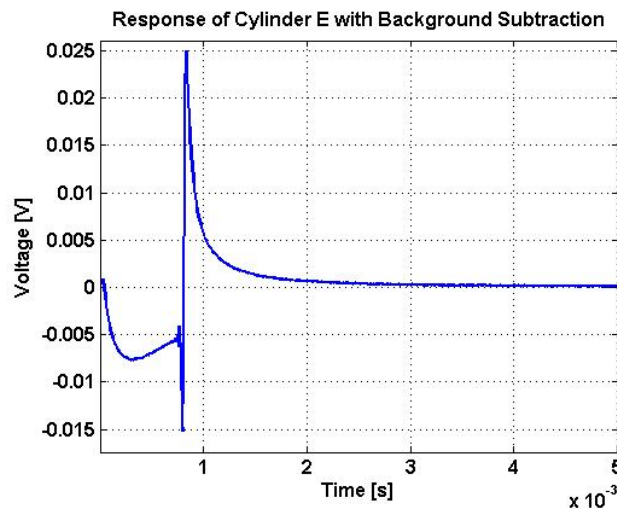
Figure 4.16 "Zoomed-in" response of Cylinder E with background subtraction

4.2.1.6 Response of Clutter

The next target tested was the clutter item. The clutter item was placed at a position, and the coils were moved in both the X- and Y-directions. For the data acquired for the clutter item, f 50 data averages were taken. Table A.6 summarizes the data acquired for the clutter item. Figure 4.17 shows a picture of the clutter item used for these

measurements. Figure 4.18 shows the data of File 13 with background subtraction for the clutter item.

Figure 4.17 Picture of the Clutter Item from Pit Testing
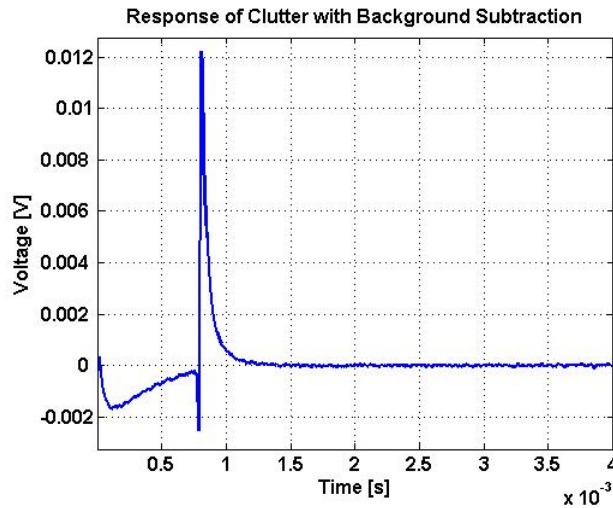
Figure 4.18 Response of Clutter Item with background subtraction (zoomed in)

4.2.2 Dynamic Testing

Dynamic testing of the EMI sensor was performed at the NRL Ordnance Classification Test Site at Blossom Point to evaluate how motion noise affects the performance of the sensor. The test field at blossom point had a 30 m X 100 m area divided into 5 lanes. Lanes are annotated A, B, C, D, and E for convenience, and each lane had 15 targets spaced 6 m from one another. A layout of the test grid is shown in

51

Figure A.4 . The dynamic tests were carried out using the MTADS trailer as well as a custom made cart. For both type of measurements, data was taken by moving the coils over Lane C shown in Figure A.4 [16]. The data acquisition for the dynamic test was carried out using a Laptop computer with DAQcard-6062E from National Instruments in the PCMCIA slot. The specifications of the data acquisition device are given in Table 3.1 in chapter three. For the dynamic test, 5 million data points were acquired as the coils were moved down Lane C.

4.2.2.1 Testing using MTADS trailer

The first part of the dynamic tests was carried out using the MTADS trailer. The details of the setup for this test are given in section A.2.1. Table A.7 gives the details of the 4 tests carried out using MTADS trailer. Figure 4.19 shows a section of the response of pass 4 from the MTADS test.
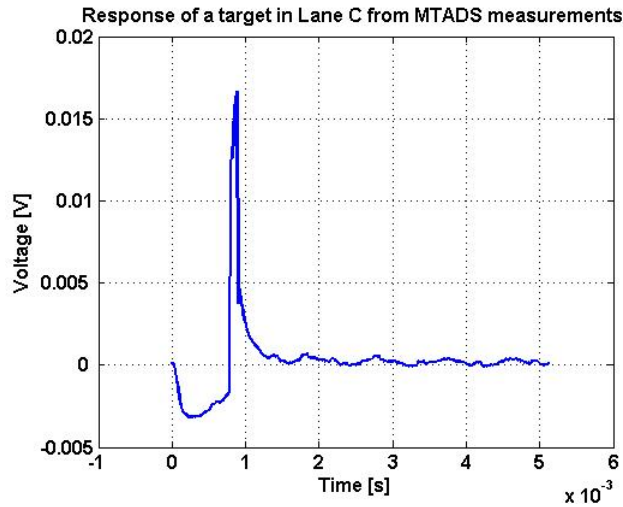
Figure 4.19 A section of the data from LaneC_Pass4 for the MTADS test

From the data it is observed that a good representation of the late time exponential decay of the target is not obtained. And also a lot of noise was observed in the MTADS data. The data acquired was not averaged and this could be one of the reasons for poor

52

data quality. Also for the MTADS test, the height of the targets with respect to the transmitter and receiver coils was more. Due to this reason, the signal level was very low and noise dominated the data obtained. Smooth function in Matlab was used to reduce the noise in the data. Methods to achieve good signal-to-noise ratio at heights of up to 1 m as well as to reduce the effects of external noise are discussed in Chapter 5.

4.2.2.2 Testing using Custom made Cart

Another dynamic test was carried out using a custom made cart. The details of the setup for this test are given in section A.2.2. Table A.8 gives the details of the 3 tests carried out using the cart. Figure 4.20 shows a section of the response from pass 1 from the cart test.
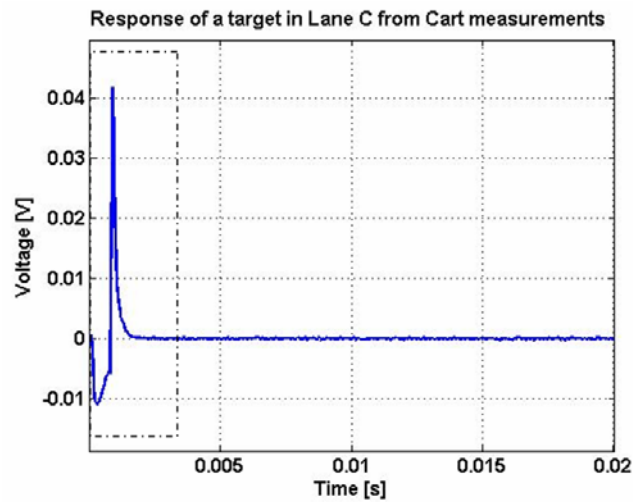
Figure 4.20 A section of the data from LaneC_Pass1

Observe that the cart-data signal level is larger than that obtained when the system was mounted on the MTADS platform. When the coils were mounted on the cart they were closer to the ground than when on the MTADS platform and for this reason higher signal-to-noise ratio was obtained. Just like the MTADS data, the cart data was not averaged and so, the smooth function in Matlab was used to reduce noise in the data. But,

even for the cart test, the exponential decay is not observed late into time, and methods to improve data fidelity in late time are discussed in Chapter 5.

Response of a target in Lane C from Cart measurements
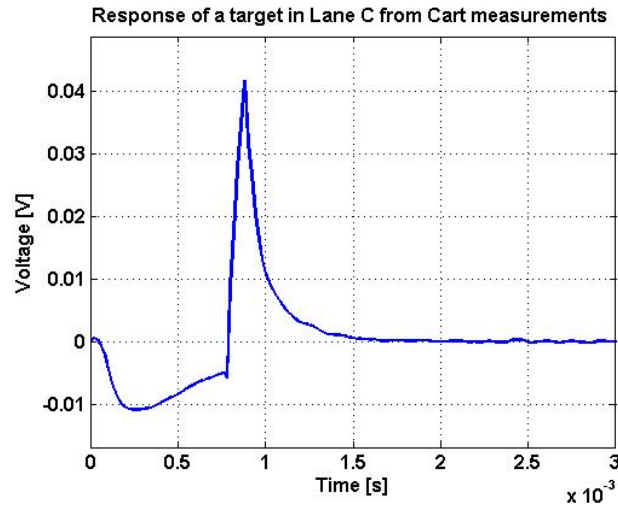
Figure 4.21 Response of Figure 4.20 zoomed on the area shown by the dotted rectangle

4.3 Summary

In this chapter, first the testing of the pulsed EMI sensor carried out in the laboratory was presented. Responses of different targets were presented, and the q-coils were analytically modeled and compared with actual responses. Also, the response of the steel cylinders was compared with the response obtained from an FEM analysis of the same. Good qualitative agreement between measured and FEM computed cylinder data helped to establish the performance bounds of the pulsed EMI system. Next, field measurements carried out at the Blossom Point Test Site in Maryland were presented.

In the field measurements stationary and dynamic tests of the pulsed EMI sensor were carried out. Responses of a variety of targets such as a 105 mm shell, 81 mm mortars etc. were presented. At this time, no analytical model exists for direct comparison to the measured data. From the data collected in the stationary tests, it is observed that the late time exponential decay of the targets was not obtained. This deficiency can be

attributed to the fact that the low frequency corner of the receiver coil amplifier was inadvertently set to high thus chocking off the late time response. From the dynamic tests, it was observed that due to low signal level, motion-induced noise dominated the data. To improve overall sensor performance, the receiver coil amplifier needs to be redesigned and the overall sensitivity of the system must also be improved.

In the next chapter, the research will be summarized, followed by suggestions for improvement and a brief overview of the work currently being done to improve performance.

CHAPTER 5   CONCLUSION

This thesis summarized the efforts towards the development of a Time-Domain (Pulsed) EMI system for detecting buried metallic objects and for discriminating between UXO and metallic clutter. Improved techniques are needed to overcome bandwidth and sensitivity limitations of the current system.

The initial chapter provided an overview of the theoretical concepts of a basic EMI system. A magnetically coupled circuit model was used to provide the analytical modeling of time- and frequency-domain EMI systems.

In Chapter 3, the frequency domain transfer function obtained in chapter two was extended to take into account the characteristics of the transmitting coil, the receiver coil, and the receiver coil amplifier. The trade-off between system dynamic range and system gain was defined. Also, the design and development of the electronics, and the data acquisition hardware for a pulsed EMI system were presented. A method of measuring the current in the receiver coil was compared to a voltage measurement technique and advantages and disadvantages of the two methods were compared.

Measurements carried out in the lab as well as the field measurements at the Naval Research Laboratory's Blossom Point test site in Maryland were described in Chapter 4.

In the lab measurements a variety of test targets such as a simple loop, and carbon steel cylinders were tested. The laboratory measurements were compared with the response obtained from Finite Element Modeling (FEM). The FEM analysis showed that important information exists for discrimination purposes in the late time response. In the field, stationary as well as dynamic tests were carried out to evaluate the performance of the sensor. A variety of targets such as the 4 inch carbon steel sphere, 105 mm shell, 81 mm mortar etc., were tested. From the stationary tests, it was observed that a good representation of the late time exponential decay of the targets was not obtained. This can be attributed to problems with the receiver coil amplifier. From the dynamic tests, it was observed that due to low sensitivity, noise dominated the data.

Currently work is in progress to overcome the problems discussed above. To increase the sensitivity of the sensor, larger receiver coils are being constructed. As the cross section of the receiver coils increases, the sensitivity of the sensor to deeply buried targets also increases. Next, the receiver amplifier used for these measurements is replaced by a current- to-voltage converter with very low input impedance. This decreases the lower break frequency of the receiver coils thereby increasing the bandwidth of the system as discussed in Chapter 3. To reduce the external noise effects as well as minimize the input offset effects, a differential current-to-voltage converter can be used. Initial measurements using a differential current-to-voltage converter have provided encouraging results. Additional tests at Blossom Point test site are planned for January 2005 in order to objectively evaluate recently completed sensor modifications.

APPENDIX A FIELD MEASUREMENTS AT THE BLOSSOM POINT TEST SITE

The purpose of visiting the Blossom Point test site in Maryland was to demonstrate the detection and discrimination capabilities of the pulsed EMI sensor. The tests were done in August 2005, for a period of 4 days. Two types of tests were carried out at the test site. The first one was a stationary test or Pit test of the EMI sensor which was carried out on a platform over a pit. The second type is a dynamic test where the EMI sensor is mounted on a flat fiberglass trailer and pulled by a truck down a lane.

A.1 Pit Measurements

Figure A.1 shows a schematic of the configuration of the pit measurement system. The apparatus consists of a test bed constructed using fiberglass material over a pit (or hole) in the ground. The test bed has a rectangular cross section with four long bars in the north-south direction and many horizontal cross pieces in the east-west direction. The outer north-south bars have a total of 40 holes numbered as hole #1, hole #2 etc. The holes are spaced 10 cm apart up to hole #34, and are spaced 20 cm thereafter. A horizontal platform sits on top of the north-south beams and can be moved along them in 10 cm or 20 cm increments. The platform has holes that can be aligned with the holes on the north-south bars and pegs are put through the holes to fix the platform to a known position. The platform has an additional small square platform on top of it that can move in the east-west direction. The frame consisting of transmitter and receiver coils is placed on top of the platform and held in place using non-metallic clamps.
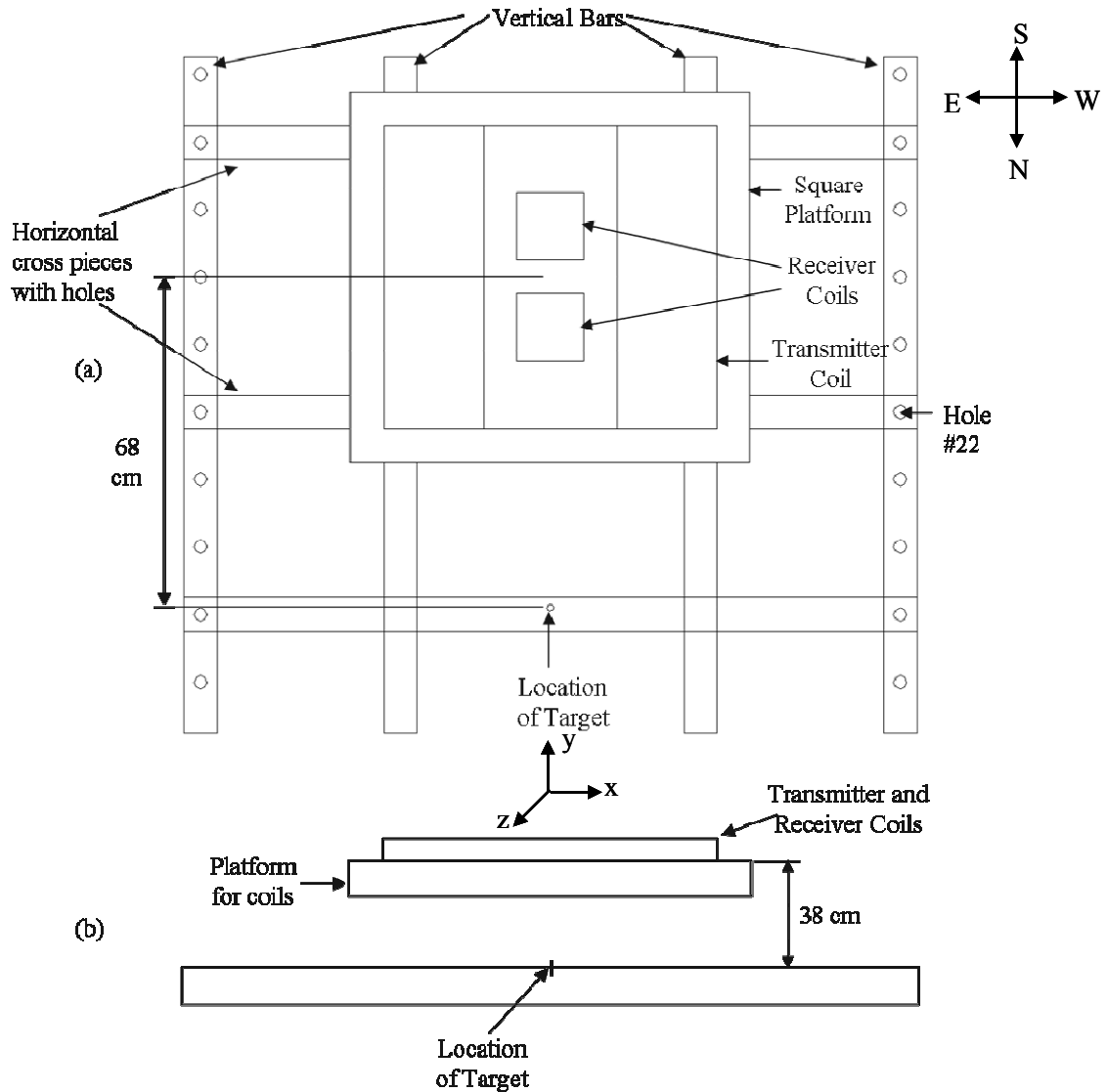
Figure A.1 Schematic of the stationary testing platform (a) Top View (b) Side View

The target is placed on a hole on an east west cross member and then the platform containing the coils is moved along the x-(east-west) and y-(north-south) directions relative to the stationary target. The distance from the center of the coils to the point where the target is placed is 68 cm when the platform is over hole #22, and the height of this point from the top of the square platform is 38 cm. The location (x, y, z) of the center of the platform relative to the hole in the east-west directed cross member is known.

59

Furthermore, the location of a target relative to the hole in the cross member has been measured and therefore the location of the target relative to the transmitter and receiver coils can be easily computed.

The "pulser" box which contains the pulse-generation circuitry along with the receiver coil signal conditioning circuitry, the oscilloscope which is used to monitor the current through the transmitter coil, and the batteries to supply power to the pulser, are placed on a wooden platform at one end of the test bed as shown in Figure A.2
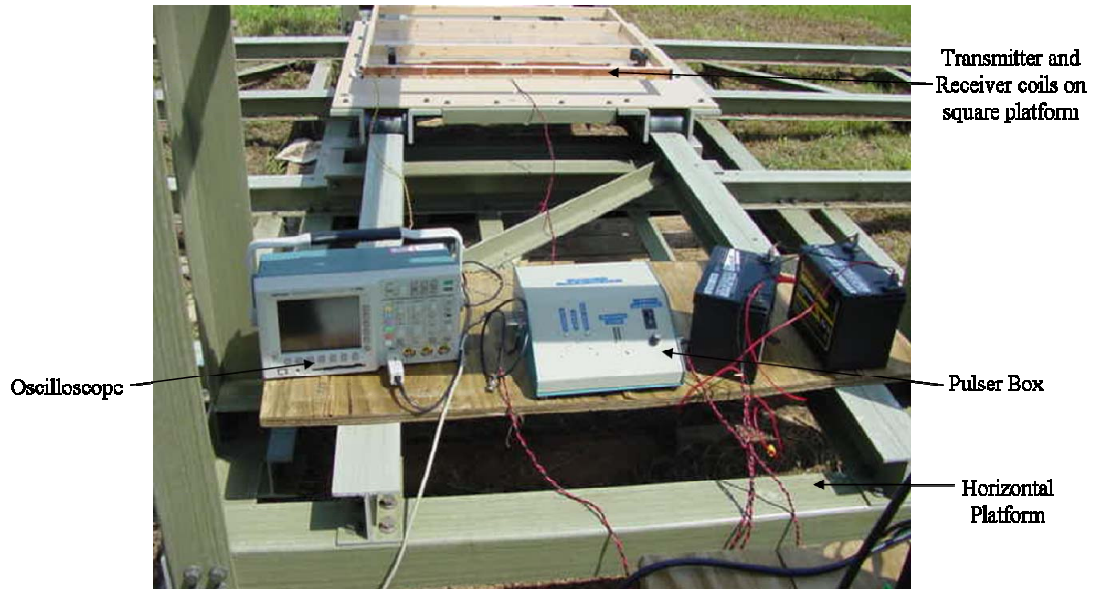
Figure A.2 Testing platform for the stationary testing

The output of the receiver signal conditioning circuit is fed to a Desktop Computer which contains a *CS-1602* A/D card from *Gage Applied Technologies* and the *Gagescope* software which comes with the A/D card was used to monitor and save the target response data. The responses of different targets were obtained for different target depths (distance from target to center of coils), and also different target positions with respect to the center of the transmitter and receiver coils.

Figure A.3 Some of the targets used in the pit test

A.1.1 Data collected for 4 inch Carbon Steel Sphere

The first target measured in the Pit testing is a 4 inch carbon steel sphere. Three different tests were done using the 4 inch carbon steel sphere and these tests are referred to as Test1, Test2, and Test3 respectively. For each test, the target was placed at some position and the platform with the transmitter and receiver coils was moved in the Y direction as indicated in Figure A.1. Data was collected at each platform position. Table A.1 shows the position of the target with respect to the center of the coils for all the three tests.

Table A.1 4 inch Carbon Steel Sphere

Data File	4 inch Carbon Steel Sphere Tests								
	Position of the Target with respect to the center of the coils								
	Test1			Test2			Test3		
	X(cm)	Y cm)	Z(cm)	X(cm)	Y(cm)	Z(cm)	X(cm)	Y(cm)	Z(cm)
File 1	0	+98	33	0	+95.5	42.5	0	+95.5	43.5
File 2	0	+88	33	0	+85.5	42.5	0	+85.5	43.5
File 3	0	+78	33	0	+75.5	42.5	0	+75.5	43.5
File 4	0	+68	33	0	+65.5	42.5	0	+65.5	43.5
File 5	0	+58	33	0	+55.5	42.5	0	+55.5	43.5
File 6	0	+48	33	0	+45.5	42.5	0	+45.5	43.5
File 7	0	+38	33	0	+35.5	42.5	0	+35.5	43.5
File 8	0	+28	33	0	+25.5	42.5	0	+25.5	43.5
File 9	0	+18	33	0	+15.5	42.5	0	+15.5	43.5
File 10	0	+8	33	0	+5.5	42.5	0	+5.5	43.5
File 11	0	-8	33	0	-5.5	42.5	0	-5.5	43.5
File 12	0	-18	33	0	-15.5	42.5	0	-15.5	43.5
File 13	0	-28	33	0	-25.5	42.5	0	-25.5	43.5
File 14	0	-38	33	0	-35.5	42.5	0	-35.5	43.5
File 15	0	-48	33	0	-45.5	42.5	0	-45.5	43.5
File 16	0	-58	33	0	-55.5	42.5	0	-55.5	43.5
File 17	0	-78	33	0	-65.5	42.5	0	-65.5	43.5
File 18	0	-98	33	0	-75.5	42.5	0	-75.5	43.5

A.1.2 Data collected for 105 mm shell

The next target measured was the 105 mm shell. For the 105 mm shell different measurements were taken with horizontal and vertical orientations of the target with respect to the axis of the coils, as well as different target depths and locations with respect to the center of the coils. Table A.2 summarizes the data acquired for the 105 mm shell. For all the tests except Test3, the number of data averages was set to 25 in the data acquisition software, and for Test3 50 averages were used.

Table A.2 Data Acquired for the 105 mm shell

Data File	105 mm shell measurements														
	Orientation of the incident magnetic field with respect to the primary axis of the target and position of the target with respect to the center of the coils respectively														
	Transverse									Axial					
	Test1			Test2			Test3			Test4			Test5		
	X (cm)	Y (cm)	Z (cm)	X (cm)	Y (cm)	Z (cm)	X (cm)	Y (cm)	Z (cm)	X (cm)	Y (cm)	Z (cm)	X (cm)	Y (cm)	Z (cm)
File1	0	+144.75	32.45	0	+143.2	41.6	-65	-81	53	0	+127.25	52	-4	+133	67.7
File2	0	+134.75	32.45	0	+133.2	41.6	-65	-41	53	0	+117.25	52	-4	+123	67.7
File3	0	+124.75	32.45	0	+123.2	41.6	-65	-1	53	0	+107.25	52	-4	+113	67.7
File4	0	+114.75	32.45	0	+113.2	41.6	-65	+39	53	0	+97.25	52	-4	+103	67.7
File5	0	+104.75	32.45	0	+103.2	41.6	-65	+79	53	0	+87.25	52	-4	+93	67.7
File6	0	+94.75	32.45	0	+93.2	41.6	-25	+79	53	0	+77.25	52	-4	+83	67.7
File7	0	+84.75	32.45	0	+83.2	41.6	-25	+39	53	0	+67.25	52	-4	+73	67.7
File8	0	+74.75	32.45	0	+73.2	41.6	-25	-1	53	0	+57.25	52	-4	+63	67.7
File9	0	+64.75	32.45	0	+63.2	41.6	-25	-41	53	0	+47.25	52	-4	+53	67.7
File10	0	+54.75	32.45	0	+53.2	41.6	-25	-81	53	0	+37.25	52	-4	+43	67.7
File11	0	+44.75	32.45	0	+43.2	41.6	+15	-81	53	0	+27.25	52	-4	+33	67.7
File12	0	+34.75	32.45	0	+33.2	41.6	+15	-41	53	0	+17.25	52	-4	+23	67.7
File13	0	+24.75	32.45	0	+23.2	41.6	+15	-1	53	0	+7.25	52	-4	+13	67.7
File14	0	+14.75	32.45	0	+13.2	41.6	+15	+39	53	0	-7.25	52	-4	-13	67.7
File15	0	+4.75	32.45	0	+3.2	41.6	+15	+79	53	0	-17.25	52	-4	-23	67.7
File16	0	-4.75	32.45	0	-3.2	41.6	+55	+79	53	0	-27.25	52	-4	-33	67.7
File17	0	-14.75	32.45	0	-13.2	41.6	+55	+39	53	0	-37.25	52	-4	-43	67.7
File18	0	-24.75	32.45	0	-23.2	41.6	+55	-1	53	0	-47.25	52	-4	-53	67.7
File19	0	-34.75	32.45	0	-33.2	41.6	+55	-41	53	0	-57.25	52	-4	-63	67.7
File20	0	-44.75	32.45	0	-43.2	41.6	+55	-81	53	0	-67.25	52	-4	-73	67.7
File21	0	-54.75	32.45	0	-53.2	41.6	+95	-81	53	0	-77.25	52	-4	-83	67.7
File22	0	-64.75	32.45	0	-63.2	41.6	+95	-41	53	0	-87.25	52	-4	-93	67.7
File23	0	-74.75	32.45	0	-73.2	41.6	+95	-1	53	0	-97.25	52	-4	-103	67.7
File24	0	-84.75	32.45	0	-83.2	41.6	+95	+39	53	0	-107.25	52	-4	-113	67.7
File25	0	-94.75	32.45	0	-93.2	41.6	+95	+79	53	0	-117.25	52	-4	-123	67.7
File26	0	-104.75	32.45	0	-103.2	41.6	×	×	×	0	-127.25	52	-4	-133	67.7

A.1.3 Data collected for 81 mm mortar

The next target tested was an 81 mm mortar. For the 81 mm mortar, measurements were

taken with horizontal and vertical orientations of the target with respect to the axis of the

coils. Table A.3 summarizes the data acquired for the 81 mm mortar. For the data

acquired for the 81 mm mortar, 25 averages were taken.

Table A.3 Data Acquired for the 81 mm mortar

Data File	81 mm mortar measurements					
	Orientation of the incident magnetic field with respect to the primary axis of the target and position of the target with respect to the center of the coils respectively					
	Transverse			Axial		
	X (cm)	Y (cm)	Z (cm)	X (cm)	Y (cm)	Z (cm)
File 1	0	+125	35.05	0	+88.5	56
File 2	0	+115	35.05	0	+78.5	56
File 3	0	+105	35.05	0	+68.5	56
File 4	0	+95	35.05	0	+58.5	56
File 5	0	+85	35.05	0	+48.5	56
File 6	0	+75	35.05	0	+38.5	56
File 7	0	+65	35.05	0	+28.5	56
File 8	0	+55	35.05	0	+18.5	56
File 9	0	+45	35.05	0	+8.5	56
File 10	0	+35	35.05	0	-8.5	56
File 11	0	+25	35.05	0	-18.5	56
File 12	0	+15	35.05	0	-28.5	56
File 13	0	+5	35.05	0	-38.5	56
File 14	0	-5	35.05	0	-48.5	56
File 15	0	-15	35.05	0	-58.5	56
File 16	0	-25	35.05	0	-68.5	56
File 17	0	-35	35.05	×	×	×
File 18	0	-45	35.05	×	×	×
File 19	0	-55	35.05	×	×	×
File 20	0	-65	35.05	×	×	×
File 21	0	-75	35.05	×	×	×
File 22	0	-85	35.05	×	×	×

A.1.4 Data collected for 40 mm shell

The next target tested was a 40 mm shell. For the 40 mm shell, measurements

were taken with horizontal and vertical orientations of the target with respect to the axis

of the coils. For the data acquired for the 40 mm shell, 25 averages were taken. Table A.4 summarizes the data acquired for the 40 mm shell.

Table A.4 Data Acquired for the 40 mm shell

Data File	40 mm shell measurements					
	Orientation of the incident magnetic field with respect to the primary axis of the target and position of the target with respect to the center of the coils respectively					
	Transverse			Axial		
	X (cm)	Y (cm)	Z (cm)	X (cm)	Y (cm)	Z (cm)
File 1	0	+98	23.2	0	+88	24.05
File 2	0	+88	23.2	0	+78	24.05
File 3	0	+78	23.2	0	+68	24.05
File 4	0	+68	23.2	0	+58	24.05
File 5	0	+58	23.2	0	+48	24.05
File 6	0	+48	23.2	0	+38	24.05
File 7	0	+38	23.2	0	+28	24.05
File 8	0	+28	23.2	0	+18	24.05
File 9	0	+18	23.2	0	+8	24.05
File 10	0	+8	23.2	0	-8	24.05
File 11	0	-8	23.2	0	-18	24.05
File 12	0	-18	23.2	0	-28	24.05
File 13	0	-28	23.2	0	-38	24.05
File 14	0	-38	23.2	0	-48	24.05
File 15	0	-48	23.2	0	-58	24.05
File 16	0	-58	23.2	×	×	×

A.1.5 Data collected for Cylinder E

The next target tested was Cylinder E. For the Cylinder E, measurements were taken with horizontal and vertical orientations of the target with respect to the axis of the coils. For each orientation measurements were taken for two different target depths with respect to the coils. Table A.5 summarizes the data acquired for Cylinder E. For the data acquired for Cylinder E, 50 averages were taken.

Table A.5 Data Acquired for the Cylinder E

Data File	Transverse						Axial					
	Test1			Test2			Test3			Test4		
	X(cm)	Y (cm)	Z(cm)	X (cm)	Y(cm)	Z(cm)	X(cm)	Y(cm)	Z(cm)	X(cm)	Y(cm)	Z (cm)
File 1	0	+163.5	41.81	0	+137.8	54.81	0	+130.5	58.94	0	131	45.24
File 2	0	+153.5	41.81	0	+127.8	54.81	0	+120.5	58.94	0	+121	45.24
File 3	0	+143.5	41.81	0	+117.8	54.81	0	+110.5	58.94	0	+111	45.24
File 4	0	+133.5	41.81	0	+107.8	54.81	0	+100.5	58.94	0	+101	45.24
File 5	0	+123.5	41.81	0	+97.8	54.81	0	+90.5	58.94	0	+91	45.24
File 6	0	+113.5	41.81	0	+87.8	54.81	0	+80.5	58.94	0	+81	45.24
File 7	0	+103.5	41.81	0	+77.8	54.81	0	+70.5	58.94	0	+71	45.24
File 8	0	+93.5	41.81	0	+67.8	54.81	0	+60.5	58.94	0	+61	45.24
File 9	0	+83.5	41.81	0	+57.8	54.81	0	+50.5	58.94	0	+51	45.24
File 10	0	+73.5	41.81	0	+47.8	54.81	0	+40.5	58.94	0	+41	45.24
File 11	0	+63.5	41.81	0	+37.8	54.81	0	+30.5	58.94	0	+31	45.24
File 12	0	+53.5	41.81	0	+27.8	54.81	0	+20.5	58.94	0	+21	45.24
File 13	0	+43.5	41.81	0	+17.8	54.81	0	+10.5	58.94	0	+11	45.24
File 14	0	+33.5	41.81	0	+7.8	54.81	0	+0.5	58.94	0	+1	45.24
File 15	0	+23.5	41.81	0	-7.8	54.81	0	-0.5	58.94		-1	45.24
File 16	0	+13.5	41.81	0	-17.8	54.81	0	-10.5	58.94	0	-11	45.24
File 17	0	+3.5	41.81	0	-27.8	54.81	0	-20.5	58.94	0	-21	45.24
File 18	0	-3.5	41.81	0	-37.8	54.81	0	-30.5	58.94	0	-31	45.24
File 19	0	-13.5	41.81	0	-47.8	54.81	0	-40.5	58.94	0	-41	45.24
File 20	0	-23.5	41.81	0	-57.8	54.81	0	-50.5	58.94	0	-51	45.24
File 21	0	-33.5	41.81	0	-67.8	54.81	0	-60.5	58.94	0	-61	45.24
File 22	0	-43.5	41.81	0	-77.8	54.81	0	-70.5	58.94	0	-71	45.24
File 23	0	-53.5	41.81	0	-87.8	54.81	0	-80.5	58.94	0	-81	45.24
File 24	0	-63.5	41.81	0	-97.8	54.81	0	-90.5	58.94	0	-91	45.24
File 25	0	-73.5	41.81	0	-107.8	54.81	0	-100.5	58.94	0	-101	45.24
File 26	0	-83.5	41.81	0	-117.8	54.81	0	-110.5	58.94	0	-111	45.24
File 27	0	-93.5	41.81	0	-127.8	54.81	0	-120.5	58.94	0	-121	45.24
File 28	0	-103.5	41.81	0	-137.8	54.81	0	-130.5	58.94	0	-131	45.24

A.1.6 Data collected for Clutter

The next target tested was the clutter item. The clutter item was placed at a known position, and the coils were moved in both the x- and y- directions. For the data acquired

for the clutter item 50 averages were used. Table A.6 shows the position of the target with respect to the center of the coils.

Table A.6 Data Acquired for the Clutter

Clutter measurements			
Data File	Position of the target with respect to the axis of the coils		
	X (cm)	Y (cm)	Z(cm)
File 1	+80	-80	40
File 2	+80	-40	40
File 3	+80	0	40
File 4	+80	+40	40
File 5	+80	+80	40
File 6	+40	+80	40
File 7	+40	+40	40
File 8	+40	0	40
File 9	+40	-40	40
File 10	+40	-80	40
File 11	0	-80	40
File 12	0	-40	40
File 13	0	0	40
File 14	0	+40	40
File 15	0	+80	40
File 16	-40	+80	40
File 17	-40	+40	40
File 18	-40	0	40
File 19	-40	-40	40
File 20	-40	-80	40
File 21	-80	-80	40
File 22	-80	-40	40
File 23	-80	0	40
File 24	-80	+40	40
File 25	-80	+80	40

A.2 Dynamic Testing

The dynamic testing of the EMI sensor was performed at the Blossom Point test site to evaluate how motion noise affects the performance of the sensor. The test field at blossom point had a 30 m×100 m area divided into 5 lanes. The lanes are named A, B, C, D, and E for convenience, and each lane had 15 targets spaced approximately 6 m from

one another. A layout of the test grid is shown in Figure A.4. The dynamic testing was performed using the MTADS trailer as well as a custom made cart. For both type of measurements, data was taken by moving the coils over Lane C shown in Figure A.4.
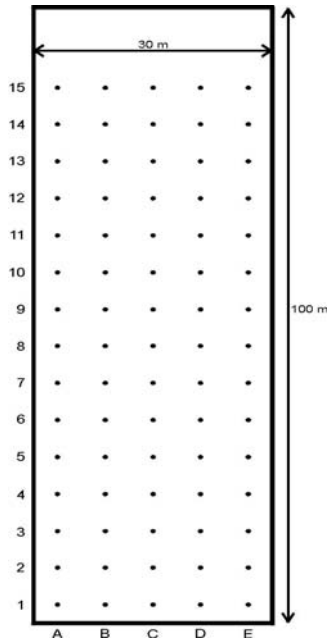
Figure A.4 Layout of the NRL ordnance classification test site at Blossom Point

A.2.1 Testing using MTADS trailer

The MTADS trailer is made of non metallic material and an all-terrain vehicle is used to tow the MTADS trailer. Figure A.5 shows the setup for dynamic testing of the EMI sensor using MTADS trailer. The EMI sensor coils were placed on the trailer at the center, and were fixed in place to prevent them from moving. The pulser box and the power supply for it were placed at one end of the trailer. A Laptop with NI DAQcard-6062E in the PCMCIA slot was used for data acquisition. Labview code was developed and used for acquiring the data.
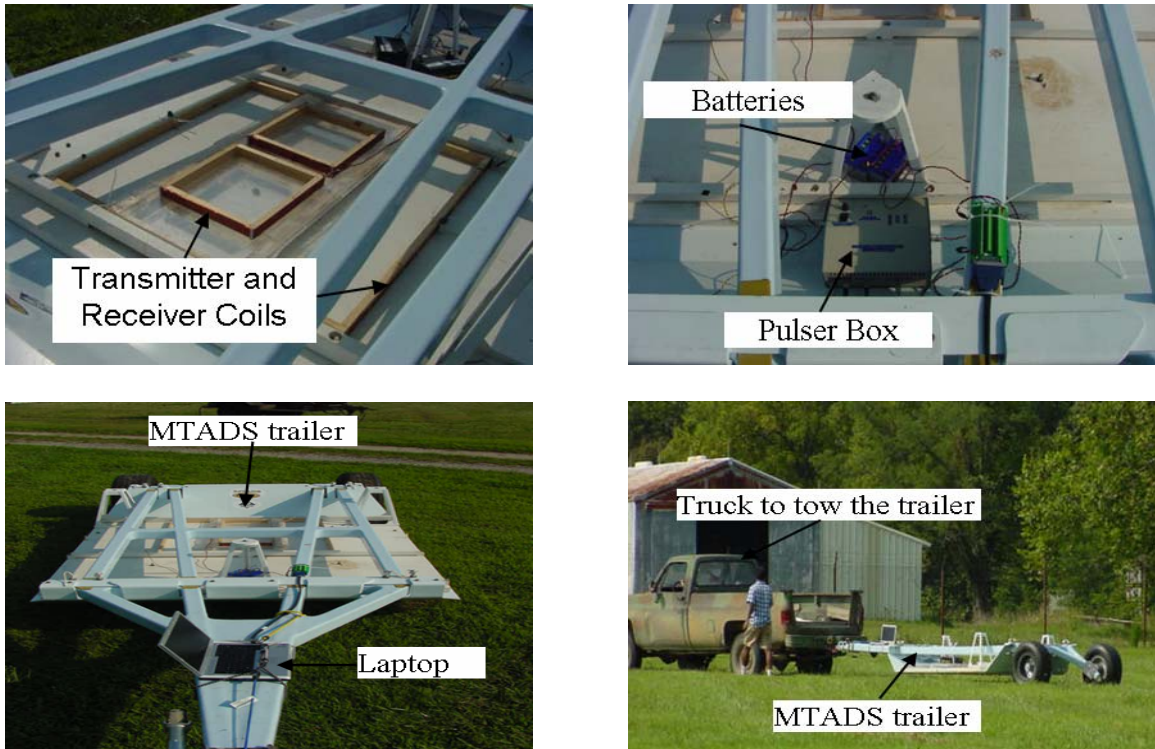
Figure A.5 Dynamic Testing of EMI sensor with MTADS trailer

The data acquisition was started at the beginning of the lane, and stopped at the end of the lane. The measurements were repeated four times and Table A.7 gives the details of the tests for each pass.

Table A.7 Details of the Dynamic Test using MTADS trailer

Pass	Direction	Pulse Rep. rate (ms)
1	S to N	10
2	N to S	10
3	S to N	10
4	N to S	10

A.2.2 Testing using Custom made Cart

The cart for performing the dynamic tests of the EMI sensor is made of non metallic fiberglass material called EXTREN. Figure A.6 shows the set up for dynamic testing of the EMI sensor using the cart.
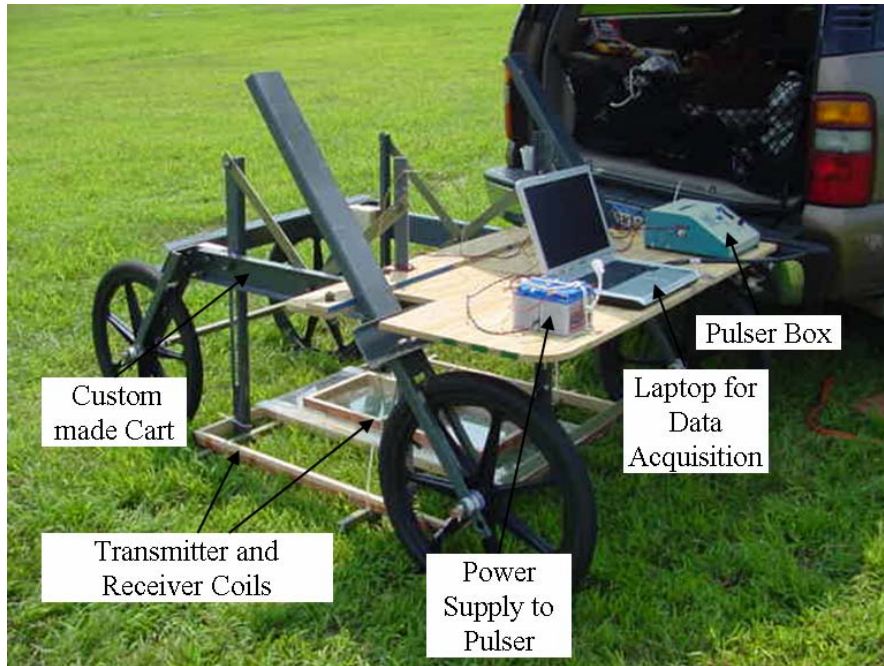
Figure A.6 Dynamic Testing of EMI sensor with Custom made cart

The cart was moved along Lane C in the test grid and data was acquired. The measurements were repeated three times, and Table A.8 gives the details of the tests.

Table A.8 Details of the Dynamic Test using the cart

Pass	Direction	Pulse Rep. rate (ms)
1	N to S	20
2	S to N	20
3	N to S	10

APPENDIX B MICROELECTROMECHANICAL SYSTEMS (MEMS) CAPACITIVE PRESSURE SENSOR ARRAY FABRICATED USING PRINTED CIRCUIT PROCESSING TECHNIQUES

Micro Electro-Mechanical Systems (MEMS) based capacitive pressure sensors are typically fabricated using silicon micromachining techniques. In this work, novel Liquid Crystal Polymer (LCP) based capacitive pressure sensors, fabricated using printed circuit processing techniques, are reported. LCP exhibits good dimensional stability, material flexibility, high chemical resistance, and extremely low moisture absorption, which makes it suitable for MEMS applications. The pressure sensor consists of a cylindrical cavity formed by a sandwich of LCP substrate, LCP spacer layer with circular holes and LCP top layer. The bottom electrode and the top electrode of the capacitive pressure sensor are defined on the top surface of the LCP substrate and the bottom surface of the top LCP layer, respectively. A typical pressure sensor with a diaphragm radius of 1.6 mm provides a total capacitance change of 0.7627 pF for an applied pressure in the range of 0-170 kPa.

B.1 Introduction

A large variety of bulk micromachined and surface micromachined pressure sensors have been developed for industrial and biomedical applications [17]-[19]. For bulk micromachining, single crystal silicon has been the predominant material of choice whereas polysilicon and low stress nitride are the two notable thin films used for surface micromachining [20].

In recent years, there has been considerable interest in the development of Microelectromechanical systems (MEMS) fabricated using printed circuit board (PCB) processing techniques combined with specialized micromachining techniques such as laser machining, plasma etching etc. [21]-[22]. The advantages of the PCB based MEMS approach include low cost, compatibility with organic substrate based Multi-chip module laminate (MCM-L) technology [23], ease of integration with embedded passives [24] and surface mount electronics, suitability for batch fabrication in large panels and high volume manufacturing. A large array of pressure sensors can be batch fabricated using roll-to-roll flexible printed circuit processing systems for large area applications.

Two types of pressure sensors commonly used in MEMS applications are: piezoresistive type and capacitive type. In this work, capacitive type pressure sensors have been developed using LCP. Capacitive pressure sensors have higher measurement sensitivity, decreased temperature sensitivity, and reduced power consumption, and better stability compared with other types of pressure sensors [25]. Capacitive pressure sensors operate on the principle of pressure induced deflection of a metallized flexible membrane and the subsequent measurement of capacitance between this flexible membrane and a fixed bottom plate [26].

In the past, pressure sensors have been fabricated using kapton Polyimide films, ceramic tape etc. Sung-Pil Chang et. al. have used a combination of micromachining and lamination techniques for fabrication of a capacitive pressure sensor using kapton polyimide film [27]. Michael A. Fonseca et. al. have used lamination techniques for the fabrication of a capacitive pressure sensor using low-temperature cofireable ceramic (LTCC) [28]. In this appendix, novel Liquid Crystal Polymer (LCP) based capacitive

72

pressure sensors fabricated using conventional printed circuit processing techniques are presented. The proposed pressure sensors are suitable for integration with system-on-package (SOP) type Microsystems fabricated using low-cost MCM-L technologies [29]. Liquid crystal polymer is a thermoplastic material with unique structural and physical properties. The advantages of LCP include low cost, versatility of fabrication such as low temperature thermal bonding, mechanical flexibility, and less moisture absorption compared to other polymer films used in MEMS processes [21].

The remainder of the appendix is organized as follows: fabrication and assembly processes for the proposed LCP based pressure sensors are discussed in Section B.2, design and experimental characterization of the pressure sensor array are presented in Section B.3, and finally concluding remarks are outlined in Section B.4.

B.2 Fabrication and Assembly

B.2.1 Sensor Configuration

The configuration of the LCP based capacitive pressure sensor is shown in Figure B.1. It consists of three layers: 30-mil thick high-temperature LCP substrate (R/flex 3850 available from Rogers Corporation) with 0.5-micron thick copper metallization, 2-mil thick high-temperature LCP top layer (R/flex 3850) with 0.5-micron thick copper metallization, and 2-mil low-temperature LCP spacer layer (R/flex 3600). The melting temperature of the high-temperature LCP substrate and the LCP top layer is 315˚C. The melting temperature of the low-temperature LCP spacer is 280˚C. The pressure sensor consists of a cylindrical cavity formed by a sandwich of the top layer (with the top electrode), the spacer layer (with the circular hole) and the substrate (with the bottom electrode). The bottom electrode and the top electrode inside the cavity form a parallel

plate capacitor configuration. The spacer layer provides the spacing between the substrate layer and the top layer. Consequently, the thickness of the spacer layer determines the initial gap between the two electrodes of the sensor. The air gap between the electrodes is 49 μm.

The circular portion of the top LCP layer located above the circular hole (diameter 2a) of the spacer layer serves as the movable diaphragm of the pressure sensor. At atmospheric pressure, the pressure sensor provides an initial capacitance, which corresponds to the undeflected position of the movable diaphragm. When the pressure (outside the sensor cavity) is increased above the atmospheric level, the diaphragm deflects downward increasing the capacitance of the sensor from the initial value.
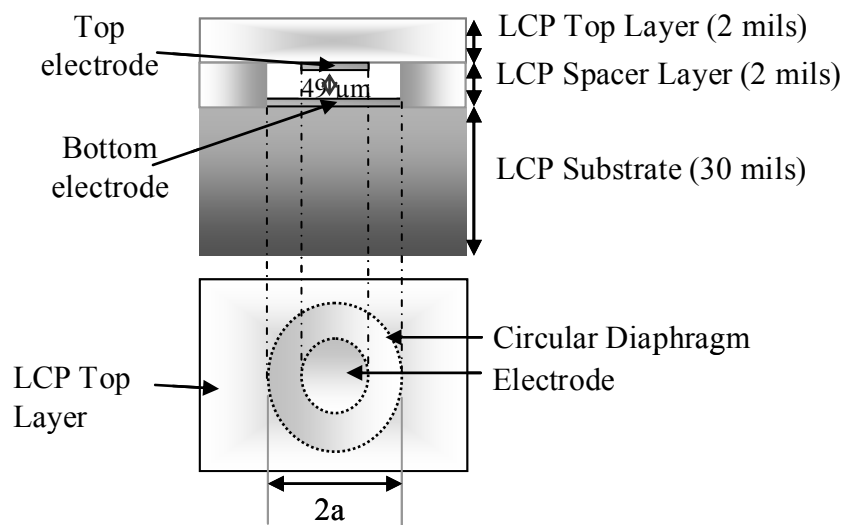

Figure B.1 LCP based MEMS capacitive pressure sensor configuration

B.2.2 Sensor fabrication

The sensor fabrication process involves two major steps. In the first step, the metallization layers on the top surface of the LCP substrate and the bottom surface of the top LCP layer are patterned by photolithography and wet etching processes to form the

bottom electrode and the top electrode of the capacitive pressure sensor, respectively. In

the second step, circular holes of various diameters in the range of 1-3 mm are machined

in the LCP spacer layer using a deep reactive ion etching (DRIE) technique.
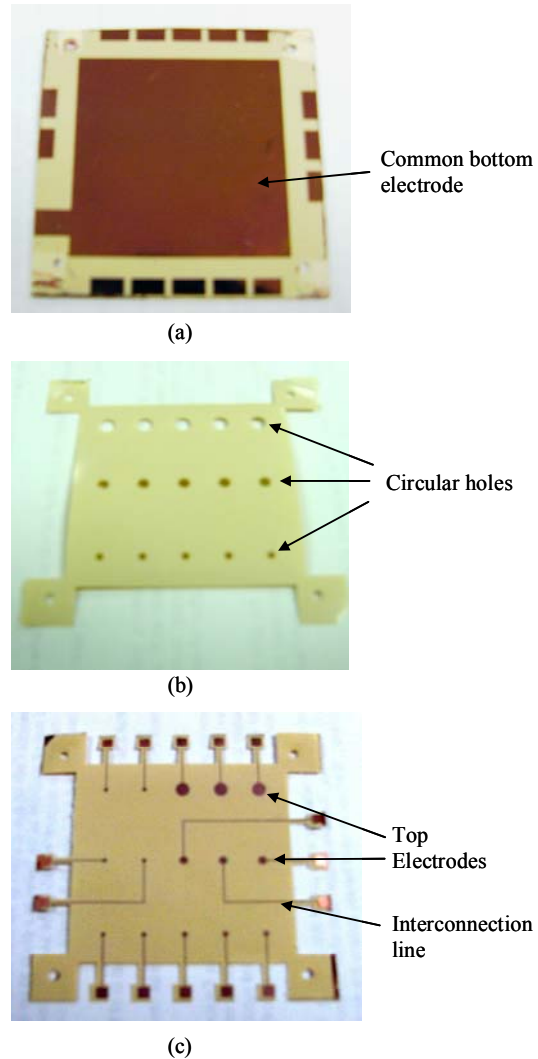

(a)

(b)

(c)

Figure B.2 Photographs of various layers of the pressure sensor array (a) LCP substrate
with a common bottom electrode, (b) LCP spacer with circular holes, and (c) LCP top
layer with copper top electrodes.

The circular segment of the top LCP layer located above the circular hole of the

spacer layer forms the movable diaphragm of the pressure sensor. Therefore, the diameter

of the movable circular membrane corresponds to the diameter of the circular hole in the spacer layer. Figure B.2 shows photographs of the three layers of the pressure sensor.

B.2.3 Lamination Process

The lamination process involves alignment of the three layers followed by a thermo-compression bonding process. Two stainless steel blocks with alignment holes and pins (shown in Figure B.3) are used to align the three layers. The sequence of the three layers after alignment is shown in Figure B.4.
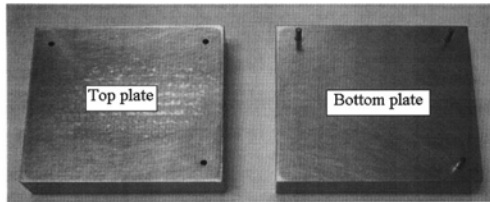

Figure B.3 Metal blocks with alignment holes and pins used in the lamination process

Thermo-compression bonding was performed using a Carver Press consisting of two rectangular aluminum platens shown in Figure B.5. The fixture consisting of two stainless steel blocks, along with the aligned layers, is placed between the press platens. Platens' heating is regulated by a temperature controller with a thermocouple.
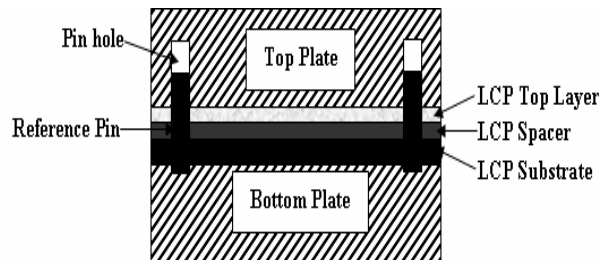

Figure B.4 Sequence of the three layers of the pressure sensor during lamination

Thermo-compression bonding is performed at a pressure of 150 psi and at a temperature of 280˚C, which is the melting temperature of the LCP spacer layer. During the bonding process, both temperature and pressure are maintained for 30 min and the
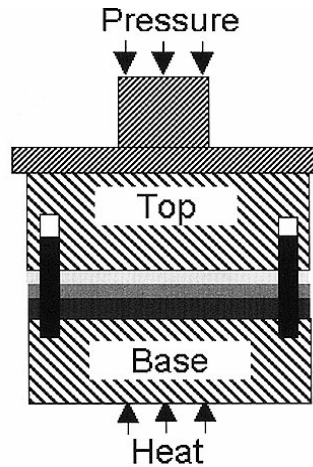
Figure B.5 Press used for thermo-compression bonding

assembly is cooled down to room temperature before the pressure is released. The

fabricated pressure sensor array is shown in Figure B.6. The fabrication and assembly

processes employed here are described in [22].

B.3 Design and Characterization

B.3.1 Design

The principle of operation of the capacitive type pressure sensor reported here is

based on the pressure induced deflection of a flexible LCP membrane with electrode and

the subsequent measurement of capacitance between the electrode on this deflecting

membrane and a fixed bottom electrode on the substrate. For analytical modeling [27],

[30], several assumptions have been made: (a) stretching of the membrane has been

neglected, since the membrane will not be undergoing deflections large compared with its

thickness; (b) residual stress in the membrane has been neglected; (c) the thickness of the

metallic electrode on the membrane has been neglected, since this thickness is small

compared with the membrane thickness; (d) electric field fringing effects of the parallel

plate configuration have been neglected, since the gap between the top electrode and the

77

fixed bottom electrode is small compared with their lateral extents. Under these conditions, if the deflection at the center of the membrane is w_0, t is the thickness of the membrane, d_1 is the initial (undeflected) gap distance between the fixed bottom electrode and the top electrode, and P is the uniform applied pressure on the membrane, then the deflection of a circular membrane with fully clamped perimeter as a function of radius, w(r), is given by:

$$w(r) = w_0 \left[1 - \left(\frac{r}{a} \right)^2 \right]^2 \qquad \text{(B.1)}$$

where a is the radius of the plate ($0 \leq r \leq a$) and the deflection at the center of the plate is given by

$$w_0 = \frac{Pa^4}{64D} \qquad \text{(B.2)}$$

In equation (B.2), D is the flexural rigidity of the membrane which is given by:

$$D = \frac{Et^3}{12(1 - v^2)} \qquad \text{(B.3)}$$

where E is the elastic modulus and v is the Poisson ratio of the membrane.

These design equations have been used for designing various pressure sensors and the experimental characterization of an example pressure sensor is discussed.

B.3.2 Experimental Characterization

B.3.2.1 Scanning Acoustic Microscope Measurements

Photograph of the fabricated 5 x 3 pressure sensor array prototype is shown in Figure B.6. The prototype consists of various pressure sensors with diaphragm diameters in the range of 2 mm to 4.8 mm. The diameter of the circular holes in the LCP spacer

78

layer for various pressure sensors has been measured using a Scanning Acoustic Microscope (SAM).
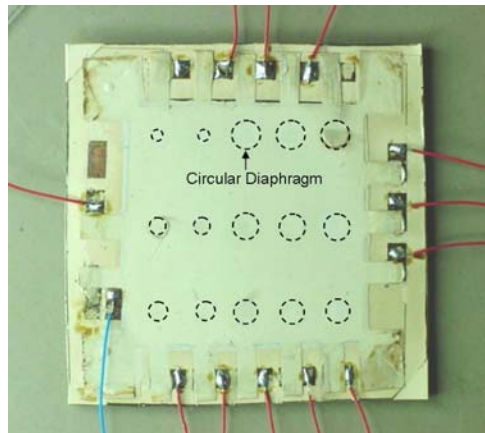

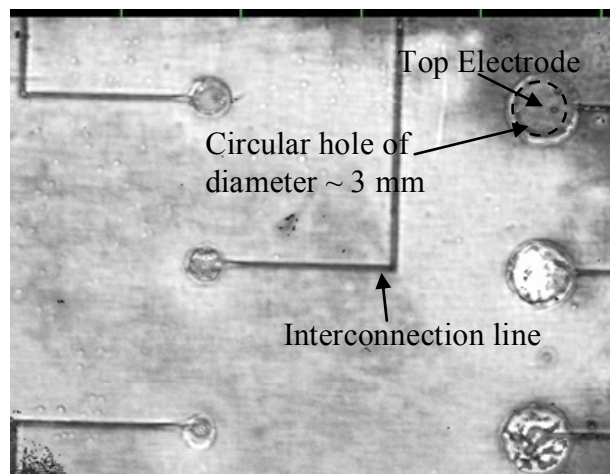Figure B.6 Photograph of a 5 x 3 capacitive pressure sensor array

Figure B.7 Scanning Acoustic Microscope (SAM) picture showing a portion of the pressure sensor array

An SAM picture of a portion of the pressure sensor array is shown in Figure B.7. A pressure sensor with an approximate diaphragm diameter of 3 mm is indicated in Figure B.7. The top electrodes and the interconnection lines of the sensor array defined on the bottom surface of the top LCP layer (refer to c)) can also be seen in the SAM picture.

B.3.2.2 Measurement Setup

The measurement setup for testing the capacitive pressure sensors is shown in Figure B.8. It consists of two components: a custom made pressure chamber and the signal conditioning circuitry. The pressure chamber is made of Teflon with dimensions of 9.5″×8.5″×3″. It has a pressure inlet connected to a pressure gauge and an outlet connected to the safety valve. As shown in Figure B.8, the pressure sensor is placed inside the chamber for characterization. When the pressure inside the chamber is above the atmospheric pressure, the movable diaphragm deflects downward, thereby increasing the capacitance between the top and bottom electrodes. The capacitance change is measured using a Capacitance-to-voltage conversion circuit discussed in the next section.
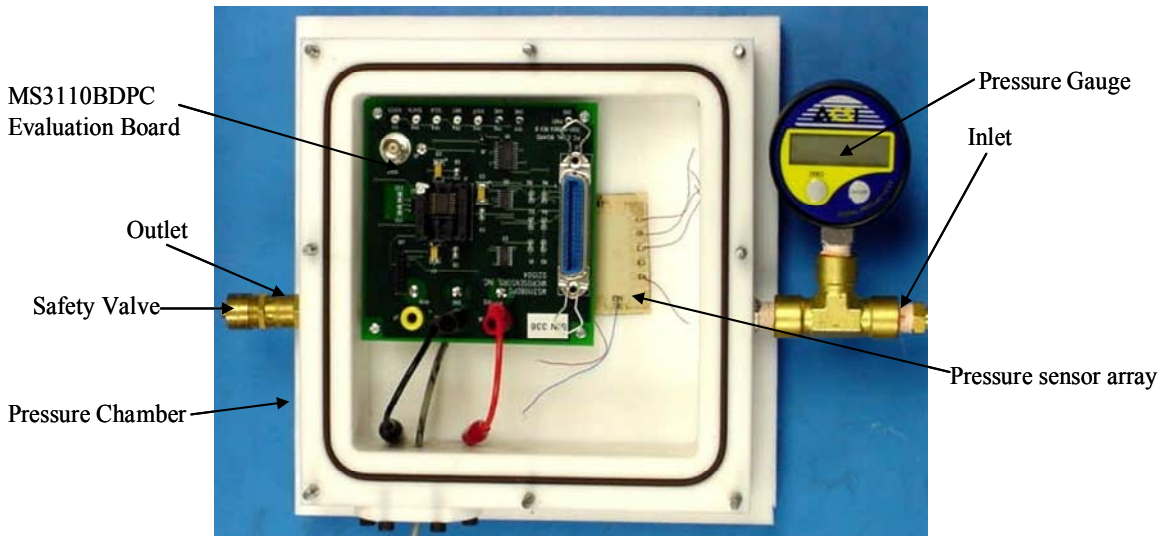

Figure B.8 Experimental setup for testing LCP based pressure sensors

B.3.2.3 Capacitance-to-voltage conversion circuit

A universal capacitive read-out (UCR) IC MS3110 is used in conjunction with its evaluation board MS3110BDPC from Microsensors Inc. as the read-out circuit. The evaluation board allows programming of the read-out IC through a parallel port cable

connected to a PC. The theory of operation of the chip can be described using the block diagram shown in Figure B.9 [31]. The MS3110 outputs a voltage proportional to the difference between the two capacitances CS1IN and CS2IN connected to the input terminals. CS1 and CS2 are the internal trim capacitances of the chip. The chip can be used either in differential mode or single-variable mode. In the single-variable mode, the sensor being tested is connected to the input terminal CS2IN of the chip and the internal trim capacitor CS1 on the other input terminal of the chip is used to compensate for any offset in the output voltage corresponding to the capacitance in the initial state of the pressure sensor. The initial capacitance of the sensor includes parasitic capacitance and the up state capacitance between the sensor electrodes. The internal trim capacitor CS1 can be varied from 0.2pF-10pF. The output voltage can be expressed as a function of the sensing capacitances $CS1_T$ and $CS2_T$ given by [31]

$$V0 = GAIN*V2P25*1.14*\left(CS2_T - CS1_T\right)/C_F + VREF \tag{B.4}$$

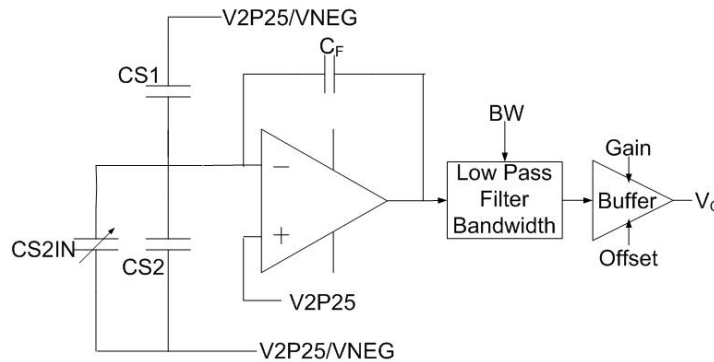where $CS1_T$=CS1, $CS2_T$=CS2IN+CS2, V2P25=VREF is the reference input voltage, which is DC 2.25 V.

Figure B.9 Block diagram of the MS3110 IC used in the single-variable mode

81

B.3.2.4 Results and Discussion

An example pressure sensor with diaphragm radius of 1.6mm is discussed here. Figure B.10 shows a plot of voltage output from the MS3110 UCR circuit. The voltage change over an applied pressure range of 0-170 kPa is 0.763V. The sensitivity is 4.8 mV/kPa and the linearity error is 6.1%. Linearity error is defined as the percentage ratio of deviation of the sensor output from a straight-line relationship over the desired pressure range to the full-scale span of the pressure sensor. In this case, the deviation was obtained using a least-squares method, and the full scale span of the sensor is defined as the difference between the output voltage at the maximum and minimum pressure, respectively, in the desired operating pressure range. The corresponding capacitance change of the pressure sensor was calculated using equation (4). Figure B.11 shows the relative capacitance change with the applied pressure. The total capacitance change of the sensor is 0.7627pF for an applied pressure in the range of 0-170 kPa.
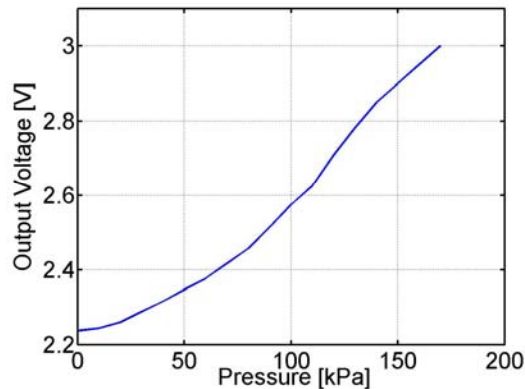

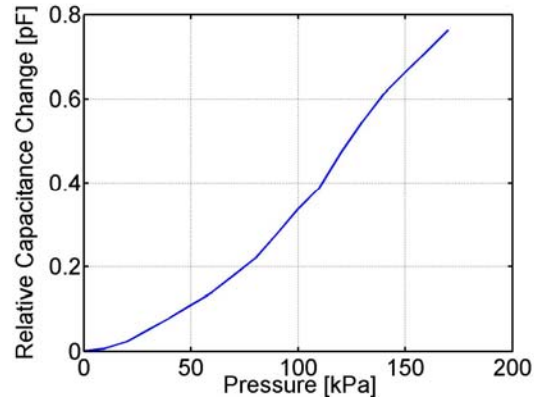Figure B.10 Output voltage from MS3110 UCR for an example pressure sensor.

Figure B.11 Relative capacitance change versus applied pressure for an example pressure sensor

B.4 Conclusion

A MEMS capacitive pressure sensor array fabricated using low cost printed circuit processing techniques is reported. An example pressure sensor with diaphragm radius of 1.6 mm that provides a total capacitance change of 0.7627 pF for an applied pressure in the range of 0-170 kPa is discussed. The sensitivity of the pressure sensor is 4.8 mV/kPa. The proposed pressure sensors are suitable for integration with system-on-package (SOP) type Microsystems fabricated using low-cost MCM-L technologies.

BIBLIOGRAPHY

[1] "Landmine Monitor Report 2004," available online at: www.icbl.org

[2] Stephen D. Billings, "Discrimination and Classification of Buried Unexploded Ordnance Using Magnetometry," *IEEE Transactions on Geoscience and Remote Sensing,* Vol. 42, No.6, June 2004.

[3] V. Gandhi, "Efforts toward Design and Implementation of a Pulsed Electromagnetic Induction System for Landmine Discrimination," Electrical Engineering Master of Science Thesis. Auburn: Auburn University, 2003.

[4] Kerry thesis, Electrical Engineering Master of Science Thesis: Auburn University, 2004.

[5] F. S. Grant and G.F. West, *Interpretation Theory in Applied Geophysics*, New York: McGraw-Hill Book Company, 1965.

[6] C. E. Baum, *Detection and Identification of Visually Obscured Targets*, Taylor and Francis, 1999 (Chapter 6).

[7] S.V. Chilaka, D.L. Faircloth, L.S. Riggs, M.E. Baginski, "A Comparison of Discrimination Capabilities of Time and Frequency Domain EMI Sensors," Proceedings of 2005 SPIE Conference, Vol. 5794, Orlando, FL, Mar 28-Apr 1, 2005.

[8] H.Frank Morrison, Alex Becker, G.Michael Hoversten, Torquil Smith, Erika Gasperikova, "Detection and Classification of Buried Metallic Objects", Annual Report, UX-1225, Lawrence Berkeley National Laboratory, January 2003.

[9] Stuart M. Wentworth, *Fundamentals of Electromagnetics with Engineering Applications*, John Wiley & Sons, 2004.

[10] L. S. Riggs, Sailaja V. Chilaka, L. Collins, L.T. Lowe and Richard Weaver, "Discrimination experiments with the U.S. Army's standard metal detector," *Radio Science*, Vol.39, 2004.

[11] L.S. Riggs, et al., "EMI Sensor Optimized for UXO Discrimination-Annual Report," *Auburn University*, January 2005.

[12] P. Kašpar, P. Ripka, "Induction Coils: voltage versus current output," *Imeko World Congress*, Vienna 2000, Vol. V, pp. 55-60.

[13] R.J. Prance, T.D. Clark, H. Prance, "Compact broadband gradiometric induction magnetometer system," *Sensors and Actuators*, Vol 76 (1999), pp. 117-121.

[14] Abhijith D. Pathak, "MOSFET/IGBT drivers theory and application," *Application Note AN002*, IXYS Corporation.

[15] L.P. Huelsman, *Handbook of operational amplifier active RC networks*, Burr-Brown Research Corporation, 1966.

[16] H.H. Nelson, J.R. McDonald, "Target shape classification using the MTADS," *Proceedings of the UXO Forum '99*, 1999.

[17] B.P. Gogoi, C.H. Mastrangelo, "A low-cost batch sealed capacitive pressure sensor," in *Proceedings of the IEEE conference on Micro-electromechanical systems,* January 1999, pp. 82-87.

[18] H.L. Chau, K.D. Wise, "An ultraminiature solid-state pressure sensor for cardiovascular catheter," *IEEE Trans Electron Dev.* 35 (1988) 2355–2362.

[19] Chavan, K.D. Wise, "Batch-processed vacuum-sealed capacitive pressure sensors," *IEEE J. Microelectromech. Syst.,* 10 (2001) 580–587.

[20] W P Eaton and J H Smith, "Micromachined pressure sensors: review and recent developments," in *Proceedings of the SPIE- The International Society for Optical Engineering*, vol. 3046, 1997, pp. 30-41.

[21] Xuefeng Wang, Liang-Hsuan Lu, and Chang Liu, "Micromachining Techniques for Liquid Crystal Polymer," in *14th IEEE international Conference on Micro Electro Mechanical Systems*, 2001. MEMS 2001, pp. 126-130.

[22] Ramesh Ramadoss, Simone Lee, Y. C. Lee, V. M. Bright, and K. C. Gupta, "Fabrication, Assembly, and Testing of RF MEMS Capacitive Switches Using Flexible Printed Circuit Technology," *IEEE Transactions on Advanced packaging*, Vol. 26, No. 3, August 2003.

[23] Philip E. Garrou and Iwona Turlik, *Multichip Module Technology Handbook*, McGraw-Hill, 1997.

[24] Richard K. Ulrich and Leonard W. Schaper, *Integrated Passive Component Technology*, IEEE Press-Wiley, 2003.

[25] Min-Xin Zhou, Qing-An Huang, Ming Qin, "Modeling, design and fabrication of a triple-layered capacitive pressure sensor," *Sensors and Actuators A*, 117 (2005) 71–81.

[26] Gregory T. Kovacs, "*Micromachined Transducers Sourcebook*," McGraw-Hill Science/Engineering/Math; 1 edition February 1, 1998.

[27] Sung-Pil Chang, and Mark G. Allen, "Demonstration for integrating capacitive Pressure sensors with read-out circuitry on stainless steel substrate," *Sensors and Actuators A,* 116 (2004), pp. 195-204.

[28] Michael A. Fonseca, Jennifer M. English, Martin Von Arx, and Mark G. Allen, "Wireless Micromachined Ceramic Pressure Sensor for High-Temperature Applications," *IEEE J. Microelectromech. Syst.,* Vol 11, No. 4, August 2002.

[29] Rao Tummala, *Fundamentals of Microsystems Packaging*, McGraw-Hill, 2001.

[30] S. Timeshenko, "*Theory of plates and Shells*," McGraw-Hill Book Company, New York, 1940.

[31] "Evaluation/Programming Board and Support Software-Operating Specifications and Users Manual," Microsensors Inc.